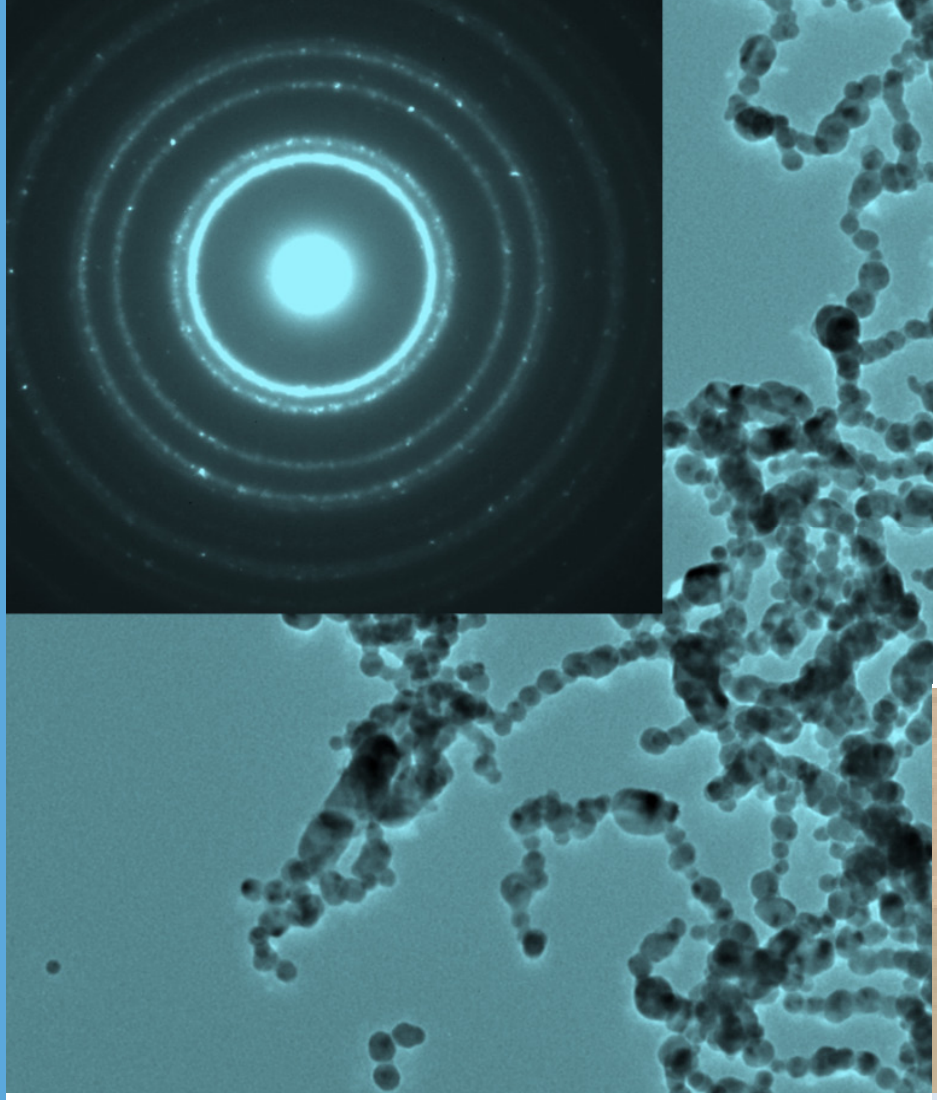

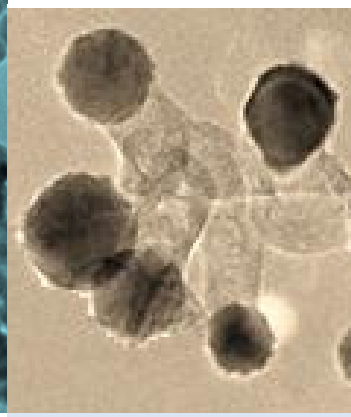

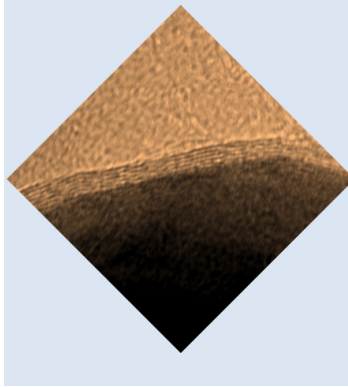

SCIENCE • TECHNOLOGY • RESEARCH HIGHLIGHTS • VISIONS

Dissertation
36

Production of Co, Ni, and Cu nanoparticles by hydrogen reduction

Johanna Forsman

VTT

VTT SCIENCE 36

Production of Co, Ni, and Cu nanoparticles by hydrogen reduction

Johanna Forsman

Thesis for the degree of Doctor of Science in Technology to be presented with due permission for public examination and debate in auditorium F239a at Aalto University School of Science and Technology (Espoo, Finland), on the 27th of August, 2013, at 12 noon.

ISBN 978-951-38-8007-1 (Soft back ed.)
ISBN 978-951-38-8008-8 (URL: http://www.vtt.fi/publications/index.jsp)

VTT Science 36

ISSN-L 2242-119X
ISSN 2242-119X (Print)
ISSN 2242-1203 (Online)

JULKAISIJA – UTGIVARE – PUBLISHER

VTT
PL 1000 (Tekniikantie 4 A, Espoo)
02044 VTT
Puh. 020 722 111, faksi 020 722 7001

VTT
PB 1000 (Teknikvägen 4 A, Esbo)
FI-02044 VTT
Tfn +358 20 722 111, telefax +358 20 722 7001

VTT Technical Research Centre of Finland
P.O. Box 1000 (Tekniikantie 4 A, Espoo)
FI-02044 VTT, Finland
Tel. +358 20 722 111, fax + 358 20 722 7001

Kopijyvä Oy, Kuopio 2013

Production of Co, Ni, and Cu nanoparticles by hydrogen reduction

Co-, Ni- ja Cu-nanohiukkasten tuotto vetypelkistysmenetelmällä. **Johanna Forsman.** Espoo 2013. VTT Science 36. 62 p. + app. 51 p.

Abstract

In this thesis, production of Co, Ni, and Cu nanoparticles by hydrogen reduction of metal chlorides in gas phase was studied. Nanoparticles have unique properties not found in bulk or micron-scale materials. These enable new products or reduced use of raw materials. Metal nanoparticle production has been studied widely, but especially for coated metal particles, research of coating mechanisms and economic production methods is still needed. The method used in this thesis combines a high yield, a high production rate, low production costs, high particle quality, and a good range of available particle number average diameters and other properties. These particles could be utilised in conductive inks, antenna substrates, medical imaging, or as sensors and catalysts.

The number average primary particle diameter (NAD) of Co particles increased from 20 to 84 nm as the particle mass concentration increased from 0.5 to 10 g/m^3. For even higher particle mass concentrations, the NAD did not increase. The Co and Cu particles were coated in-situ with carbon, by adding ethene to the reaction flow. Copper particles were also coated with carbon and carbon nanotube-like structures by adding ethene and water to the reaction flow. When ethene concentration was increased from zero to 9.2 mol-%, the NAD decreased from 84 to 17 nm for cobalt. Particle mass concentration was 10 g/m^3 or higher in these experiments. The standard deviation was 17 nm when NAD 84 nm and 7 nm when NAD was 17 nm. For copper, the NAD increased from 20 to121 nm. The particles were crystalline with an FCC structure in all cases.

The particle growth was modelled in a simplified way. It appears, that surface reaction is an important part of the particle growth process. The most likely scenario is that first, seed particles form by gas phase reaction and nucleation. Then, these particles grow partly by surface reaction and partly by condensation growth. In the gas phase, some backward reaction of metal to metal chloride occurs.

The saturation magnetic moment of the Co and Co+C particles was 141–147 emu/g, which is close to bulk Co (159 emu/g). No hysteresis was observed for these particles. Cobalt particles with and without carbon coating were used to fabricate polymer composites, which could be applied in RF antennae. The relative permeability of the composite was increased from 1 to 3 as the loading of the particles increased from zero to 28 vol-%.

Copper particles coated with carbon coating and CNT-like structures were used to fabricate inkjet fluid capable of producing conductive lines after printing a single layer. The best achieved conductivity was 6.4 S/m.

Keywords cobalt, copper, nickel, nanoparticles, core-shell, magnetic nanoparticles

Co-, Ni- ja Cu-nanohiukkasten tuotto vetypelkistysmenetelmällä

Production of Co, Ni, and Cu nanoparticles by hydrogen reduction. **Johanna Forsman.** Espoo 2013. VTT Science 36. 62 s. + liitt. 51 s.

Tiivistelmä

Tässä väitöskirjatyössä on tutkittu kobolttі-, nikkeli- ja kuparinanohiukkasten tuottoa vetypelkistysmenetelmällä kaasufaasissa. Nanomateriaaleilla on ominaisuuksia, joita ei ole vastaavilla isomman kokoluokan materiaaleilla. Niiden avulla voidaan tehdä uudenlaisia tuotteita tai vähentää materiaalien käyttöä ratkaisevasti. Lähtöaineena on käytetty metalliklorideita. Metallinanohiukkasten tuottoa on tutkittu paljon, mutta erityisesti päällystettyjen hiukkasten tapauksessa tarkkoja ja taloudellisia menetelmiä on edelleen syytä tutkia ja kehittää. Tässä työssä käytetyllä menetelmällä voidaan tuottaa hiukkasia niin, että hiukkaskoon ja muita muuttujia voi valita samalla, kun hiukkasten laatu ja tuotto pysyvät korkealla.

Kobolttihiukkasten lukumääräkeskiarvostettu primäärihiukkashalkaisija (LKH) kasvoi 20 nanometristä 84 nanometriin, kun hiukkasten massakonsentraatio kasvoi arvosta 0,5 g/m^3 arvoon 10 g/m^3. Tätä suuremmilla massakonsentraatioilla hiukkaset eivät enää kasvaneet. Koboltti- ja kuparihiukkaset päällystettiin hiilellä lisäämällä eteeniä reaktiovirtaukseen. Kuparihiukkaset päällystettiin lisäksi hiilellä ja hiilinanoputkimaisilla rakenteilla lisäämällä eteeniä ja vettä reaktoriin. Kun eteenipitoisuus kasvaa nollasta 9,2 mooliprosenttiin kobolttihiukkasten LKH pienenee 84 nanometristä 17 nanometriin. Hiukkasten massakonsentraatio oli 10 g/m^3 tai suurempi. Kun hiukkasen LKH oli 84 nm, oli keskihajonta 17 nm. Kun LKH oli 17 nm, oli hajonta puolestaan 7 nm. Kuparin kohdalla LKH pieneni 121 nanometristä ilman eteeniä 20 nanometriin, kun eteenipitoisuus nousi 9,2 mooliprosenttiin. Kaikissa tapauksissa hiukkaset olivat kiteisiä ja kiderakenne oli FCC.

Hiukkasten muodostumisprosessia mallinnettiin yksinkertaisella laskennalla. Vaikuttaa siltä, että pintareaktiolla on tärkeä osa hiukkasten kasvussa. Ensin muodostuvat hiukkasten ytimet kaasufaasireaktiolla ja nukleaatiolla. Sitten hiukkaset kasvavat kondensaatiolla ja pintareaktiolla. Kaasufaasissa tapahtuu myös jonkin verran käänteisreaktiota metallista metallikloridiin.

Sekä kobolttihiukkasten että hiilipäällystettyjen kobolttihiukkasten saturaatiomagnetisaatio vaihteli välillä 141–147 emu/g. Koboltin ominaissaturaatiomagnetisaatio on 159 emu/g. Mitatuilla hiukkasilla ei havaittu hystereesiä. Sekä hiilipäällystettyjä että päällystämättömiä kobolttihiukkasia käytettiin polymeerikomposiitin valmistuksessa. Komposiittia voidaan hyödyntää RF-antennin alustana. Komposiitin suhteellinen permeabiliteetti kasvoi arvosta 1 arvoon 3, kun hiukkasten osuus kasvoi nollasta 28 tilavuusprosenttiin.

Hiilellä ja hiili-hiilinanoputkiyhdistelmällä päällystettyjä kuparihiukkasia käytettiin valmistettaessa mustetta, jolla tehtiin johtavia viivoja tulostamalla yksi kerros mustesuihkutulostuksella. Paras johtavuus oli 6,4 S/m.

Avainsanat cobalt, copper, nickel, nanoparticles, core-shell, magnetic nanoparticles

Preface

The work presented in this thesis is the result of many projects over several years. VTT Technical Research Centre of Finland is highly appreciated for funding and support. Tekes, European Comission and OMG Kokkola Chemicals are also acknowledged for funding parts of the work.

Professor Jorma Jokiniemi, the instructor of the thesis, is highly appreciated for guidance throughout the work. Thesis supervisor, professor Esko Kauppinen, is acknowledged especially for the final stages of the journey.

I have had the pleasure to work at VTT Fine Particle team. I appreciate all former and present team members for their help and a nice atmosphere. I am grateful to Ari Auvinen for instruction and help during all stages of the thesis work. Dr Unto Tapper has taken numerous great SEM and TEM images for this thesis. Pipsa Mattila has been a great collegue especially in the laboratory. Raoul Järvinen has been a huge help while constructing the experimental setups. Several people working at VTT but not in Fine Particle team have also helped me in the process. Tuula Kajolinna and Kauko Tormonen have taught me how to use FTIR. Kim Eiroma is appreciated for fruitful co-working towards conductive inks. Professor Sebastiaan van Dijken from Aalto University is acknowledged for measuring the magnetic properties of the particles. I wish to thank also all the co-authors that were not given credit separately.

I would like to thank my pre-examiners, professor Jyrki Mäkelä and professor Ritva Serimaa for their constructive comments on finalising the thesis.

Finally, very special thanks go to my family, Lauri, Roope and Oskari, for love, support and a balanced life.

May 7th 2013, Espoo

Johanna Forsman

Academic dissertation

Instructor	Prof. Jorma Jokiniemi Biologinkuja 7 P.O. Box 1000 02044 VTT, Finland
Supervisor	Prof. Dr. Esko Kauppinen Puumiehenkuja 2 P.O. Box 15100 00076 Espoo, Finland
Reviewers	Prof. Jyrki Mäkelä Korkeakoulunkatu 3 P.O. Box 692 33101 Tampere, Finland
	Prof. Ritva Serimaa Gustaf Hällströmin katu 2 P.O. Box 64 00014 Helsingin yliopisto, Finland
Opponent	Dr Robert Grass ETH Zürich, HCI E111 Wolfgang-Pauli-Strasse 10 CH-8093 Zürich

List of publications

This thesis is based on the following original publications, which are referred to in the text as I–IV.The publications are reproduced with kind permission from the publishers

I Forsman, J., Tapper, U., Auvinen, A. and Jokiniemi, J. Production of cobalt and nickel particles by hydrogen reduction. Journal of Nanoparticle Research, 10, 2008, pp. 745–759.

II Koskela, P., Teirikangas, M., Alastalo, A., Forsman, J., Juuti, J., Tapper, U., Auvinen, A., Seppä, H., Jantunen, H., Jokiniemi, J. Synthesis of cobalt nanoparticles to enhance magnetic permeability of metal-polymer composites. Advanced Powder Technology, 22, 2011, pp. 649–656.

III Forsman, J., Koskela, P., Auvinen, A., Tapper, U., van Dijken, S., Jokiniemi, J. In-situ coated nanomagnets. Powder Technology, 233, 2013, pp. 15–21.

IV Eiroma, K., Forsman, J., Hult, E.-L., Auvinen, A., Sipiläinen-Malm, T., Alastalo, A., Tapper, U., Leppäniemi, J., Mattila, P., Lyyränen, J., Sarlin, J., Jokiniemi, J., Mössmer, S. Water-based carbon-coated copper nanoparticle fluid – formation of conductive layers at low temperature by spin coating and inkjet deposition. Journal of Imaging Science and Technology, 56(4), 2012, pp. 40501-1–40501-10.

Author's contributions

For publication I, the author has written the paper, constructed the experimental setups, carried out the experiments, and participated actively in the analysis of the results.

The author designed the carbon-coating process for publication II, carried out the carbon-coating experiments, and participated in the writing of the paper and analysis of the results.

For publication III, the author has written the paper, designed and carried out most of the experiments on carbon-coated particles, and analysed the results with help of the co-authors.

The author designed and carried out the majority of the nanoparticle synthesis experiments for publication IV and developed the method for formation of CNT-like structures on the particles. The author also wrote the particle production and analysis sections and parts of introduction and conclusion for the publication.

Contents

Appendices of this publication are not included in the PDF version. Please order the printed version to get the complete publication (http://www.vtt.fi/publications/index.jsp).

List of acronyms and symbols

a.u.	arbitrary units
BET	Brunauer-Emmet-Teller
c.	conversion
CNT	carbon nanotube
CVD	chemical vapour deposition
DIW	de-ionised water
EGBE	ethylene glycol monobuthyl ether
EGME	ethylene glycol monomethyl ether
FESEM	field-emission scanning electron microscopy
FTIR	Fourier-transform infrared spectroscopy
NAD	number average diameter of primary particles, nm
NTP	normal temperature and pressure, 273.15 K, 1 bar
RF	radio frequency
SAED	selected area electron diffraction
SEM	scanning electron microscope or scanning electron microscopy
SD	standard deviation
SSA	specific surface area, m^2/g
TEM	transmission electron microscope or transmission electron microscopy
TGA	thermo gravimetric analysis
XRD	x-ray diffraction
XRF	x-ray fluorescence

A	pre-exponential factor, 1/min
$A_{particle}$	particle surface area m^2
B	magnetic flux density, T
$[Co]$	molar concentration of Co $1/m^3$
$[CoCl2]$	molar concentration of $CoCl_2$
c_m	particle mass concentration kg/m^3
c_n	particle number concentration $1/m^3$
$c_{p,N2}$	heat capacity, kJ/kg·K
d	diameter, m
E	efficiency
E_A	activation energy, J
f	formation rate of atoms through reaction, $1/m^3s$
H	magnetic field, A/m
H_f	heat of fusion, J/kg
H_S	coercive field, mT
H_v	heat of vaporisation J/mol
k	Boltzmann's constant, $1.3806 \cdot 10^{-23}$ J/K
k_1', k_2, k_3'	reaction rate constants, m^3/s
k_1	reaction rate constant, 1/min
k_3	reaction rate constant m^6/s
m	mass, kg
M	molar mass, g/mol
M_m	mass magnetisation, emu/g or Am^2/kg
M_R	remanent magnetisation, emu/g
M_s	saturation magnetisation, emu/g
M_v	volume magnetisation, emu/cm^3 or A/m
N_A	Avogadro's constant $6.022 \cdot 10^{23}$ 1/mol
$n_{Co,s}$	number of surface atoms per particle
P	heat flux, J/s
p	pressure, Pa

p_s	saturation vapour pressure, Pa
r	radius, m
R	gas constant, 8.314 J/mol·K
T	temperature, K
$T_{b,bulk}$	bulk boiling point temperature, K
T_m	melting point temperature, K
$T_{m,bulk}$	bulk melting point temperature, K
t	time, s
v	reaction rate 1/s
V	volume, m^3
γ	surface tension, N/m
ε	emissivity
μ	permeability, H/m
μ_0	permeability of vacuum, $4\pi \cdot 10^{-7}$ N/A^2
μ_R	relative permeability, dimensionless
$\tan \delta\mu$	magnetic loss tangent, dimensionless
ρ	density, kg/m^3
σ	solid-liquid surface energy, J/m^2
σ_{SB}	Stefan-Boltzman constant, $5.7 \cdot 10^{-8}$ W/m^2K^4

1. Introduction

1.1 State of the art in Co, Ni, and Cu nanoparticle production

Metal nanoparticles have been studied for decades as they have properties not found in the same material in bulk form. The nanosize affects greatly the ratio of surface atoms to atoms deep in the crystal matrix. Therefore, surface effects are observed to a much greater extent. A notable example is catalysis, where a large surface area to volume ratio is a key parameter. Special nanoeffects are seen in nanomagnets as explained below. In addition, processing techniques like printing are not available or reasonable with micron-sized particles.

Fine cobalt, nickel and copper powders have been produced using various techniques for decades, including hydrogen reduction (Dugleux and De Almeida Marques 1980). The purity of the powders has greatly increased and nowadays particles in the nanoscale are produced with relative ease (Jang et al. 2004). Several companies, such as Alfa Aesar, Applied Nanotech, MKnano, MTI Corporation, NaBond Technologies, Nanoshel, Nanostructures, and Amorphous Materials, offer cobalt, nickel, and copper nanoparticles with and without carbon coating. The number average primary particle diameter may be chosen from several alternatives. The price varies from about €2/g to €200/g, depending on the average primary particle diameter, the width of the size distribution, and the quality of the surface coating. The available batch size varies from 1 g to several kg. The most expensive particles are characterised by narrow size distribution and a graphitic coating. Therefore, research on economical production methods of coated cobalt, nickel, and copper nanoparticles is still required.

The most active line of production technologies is plasma processes. A great variety exists within various plasma processes; a review is given by Vollath (2007). A typical metal precursor is either metal wire or metal powder. Large quantities can be produced efficiently at atmospheric pressures by RF or microwave plasma. In these systems, aggregation occurs and size distribution is wide but prices are the lowest, €2/g to €5/g (2012 quote).

The aggregation can be reduced and size distribution controlled by using low-pressure microwave plasma. In-situ carbon coating is also possible (Jun et al. 2011). In this case, the method is called plasma chemical vapour synthesis.

The price range increases to €15/g and above. However, a narrow size distribution is not obtained for the coated particles.

The second important class of synthesis techniques is based on laser evaporation. This may occur either in liquid or in the gas phase. In the latter, the energy of the laser evaporates metal from a solid target. Nanoparticles nucleate from the gaseous metal. In the gas phase, sintering and agglomeration of the particles occurs, but again, prices are in the same range as for plasma processes. In the liquid phase, metal powder is suspended in a liquid transparent to the laser wavelength. Particle size may be accurately controlled with surfactants. The prices are very high: several hundred euros per gram or even higher. However, for particles with very narrow tuneable size distribution, there are no commercial alternatives.

Coating of metal nanoparticles greatly increases their value, since oxidation resistance is improved. In addition, carbon coating decreases the surface energy of the particles, facilitates chemical bonding to organic materials, and affects the electro-magnetic properties of the produced material. In biological applications, coating also decreases the toxic effects of the metal nanoparticles. In addition, the range of methods for implementing the particles in the chosen applications is much wider. Therefore, carbon is a common surface coating material for metal nanoparticles. It has been employed, for example, by Athanassiou et al. (2006), Bonard et al. (2001), Narkiewicz et al. (2010), Schaper et al. (2004), Wang et. al. (2003), Zhai et al. (2011) and Tomita et al. (2000). The carbon coating on the particles may be tens of nanometres thick and amorphous (e.g. Schaper et al. 2004, Narkiewicz et al. 2010), or graphitic, as in this thesis (e.g. Wang et al. 2003, Tomita et al. 2000 or Bonard et al. 2001). Other coating materials include silica and polymers. Often they are applied separately from particle production (Fu, Yang et al. 2006) or by aqueous methods (Eggeman et al. 2006). When magnetic applications or conductive inks are considered, a high mass concentration of metal and thus a thin layer of carbon is preferred.

This research started with the development of a hydrogen reduction method for pure cobalt and nickel nanoparticles (Publication I). Later, the method was improved, a graphitic carbon-coating method developed, and Co nanoparticles applied for antenna substrates (Publication II). Then, the carbon-coating method was studied in detail and magnetic properties of the particles were measured (Publication III). Finally, copper particles were produced and coated with carbon. These particles were used to produce a conductive ink (Publication IV). The aim has been to develop a technique that enables cost-effective production of coated cobalt, nickel, and copper nanoparticles with a desired particle size distribution.

1.2 Properties of metal nanoparticles

In this chapter, the properties of metal particle that are measured in this thesis and relevant for the applications in this thesis are presented. Size is a crucial parameter in many applications, especially when size decreases below about 20 nm. In this thesis, the size of the particles is the number average diameter NAD of the

primary particles retrieved from TEM or SEM images. In other studies, it may be average crystal size from XRD data, average diameter from optical measurements, or average diameter from differential mobility measurements.

In addition to the average diameter, the size distribution is often described by giving the standard deviation of the average size. However, for a bimodal distribution, the average diameter and standard deviation do not alone give an accurate description of the size distribution.

Especially in catalytic applications, very high surface areas are desired and specific surface areas are routinely measured for nanoparticles. However, if pure, well-crystallised nanoparticles are preferred; the representative surface area is that given by the diameter and smooth sphere assumption. This is the case for magnetic applications. Surface coatings may have a large effect on the specific surface area.

The basic magnetic characterisation of a nanoparticle powder covers saturation magnetisation m_S, remanent magnetisation, and coercive field. These values are measured by measuring the magnetic flux *B* generated when the sample is placed in a magnetic field *H* and the field intensity is increased and decreased alternately. The magnetic flux is the sum of the magnetising force and magnetisation

$$B = \mu_0(H + M_V) \tag{1}$$

The mass magnetisation M_m is given by

$$M_m = \frac{M_V}{\rho} \tag{2}$$

The maximum of the flux density gives the saturation magnetisation of the material. The remanent magnetisation is the magnetisation of the material when the magnetising field is decreased back to zero. The opposite magnetising field required to bring the magnetic flux to zero is called the coercive field. These quantities are illustrated in Figure 1.1.

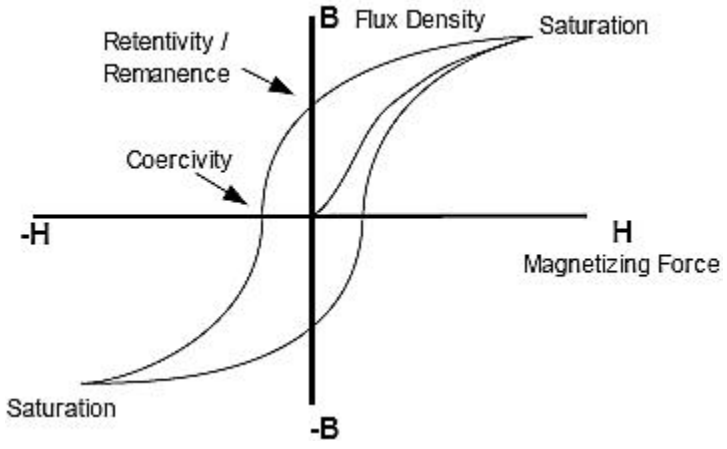

Figure 1.1. Hysteresis curve illustrating the basic magnetic quantities of a magnetic material. The measurement starts at zero magnetising force and zero flux density.

Permeability μ is defined as:

$$\mu = \frac{B}{H} \tag{3}$$

Often, relative permeability μ_R is given as:

$$\mu_R = \frac{\mu}{\mu_0} = \frac{1}{\mu_0}\frac{\mu_0(H + M_V)}{H} = 1 + \frac{dM_V}{dH} \tag{4}$$

Here, μ_0=1.25664·10^{-6} N/A^2 is the permeability of the vacuum. For ferromagnets, the largest tangent of the hysteresis curve is typically given as the permeability. A range of values from that maximum to zero exist along the hysteresis curve. Defining a single permeability number for a ferromagnet is challenging, and many methods for deriving one are available. Detailed discussion is available, for example, by Williams (2012).

The permeability of a material may be given in complex form by:

$$\mu = \mu' + i\mu'' \tag{5}$$

Then the magnetic loss tangent is given by:

$$\tan\delta_\mu = \frac{\mu''}{\mu'} \tag{6}$$

This loss tangent measures the dissipation of energy to magnetic losses.

Ferromagnetic materials are divided into hard and soft materials. Soft magnetic materials have a low remanent magnetisation, a low coercive field, and a high

permeability. Hard ferromagnetic materials have a high remanent magnetisation, a high coercive field, and a low permeability. Soft ferromagnetic materials are used, for example, for recording heads and as inductor cores. Hard magnetic materials are used, for example, for permanent magnets and recording media.

The magnetic properties change as the particle size decreases. For large particles, magnetic properties are similar to bulk magnetic properties. As particle size decreases, the particles become single domain, as it is not energetically favourable to have a domain wall within the particles. For Co, the single domain diameter is theoretically 58 nm, but the exact particle shape and crystal structure have large effects (Gubin 2009). The coercivity for single domain particles is higher than for the bulk, and saturation magnetisation is the same. Very small particles may be in s superparamagnetic state. Then, magnetisation can randomly change direction due to thermal fluctuations. The time for this direction change is called the Néel relaxation time. In the absence of an external magnetic field, the time used to measure the magnetisation of the nanoparticles is typically much longer than the Néel relaxation time. Then, the magnetisation appears to be zero: and the particles are said to be in a superparamagnetic state. In this state, an external magnetic field is able to magnetise the nanoparticles. The critical radius for superparamagnetic behaviour is 16 nm for cobalt (Gubin 2009). Bonard et al. (2001)) did not observe superparamagnetic behaviour for 5–45 NAD Co+C particles. On the other hand, Shao et al. (2006) did observe this for Co particles with various coatings. The reason for the absence of superparamagnetism for Bonard et al. (2001). is likely the wide size distribution of the particles. Even for the particles with the smallest number average particle diameter, the mass fraction of larger particles is significant. The increased saturation moment of Co nanoparticles as compared to the bulk is reported several times for particles less than 10 nm, for example by Chen et al. (1995). It is also predicted in the literature (Gubin 2009).

1.3 Applications of Co, Ni, and Cu nanoparticles

Two applications are studied in this thesis: antenna substrates for RF devices (cobalt particles) and conductive inks (copper particles). A magnetic core-shell particle with a high saturation magnetisation and a high permeability but limited dielectric losses could be used in composites for power electronics and telecommunications. The high permeability of a polymer substrate with Co nanoparticles can be utilised to minimise RF antenna size (Raj et al. 2011). This type of substrate was also fabricated in this thesis.

On the other hand, electromagnetic shielding materials can be greatly improved using nanomaterials. The RF absorption properties are optimised for high saturation magnetisation and high complex permeability at high frequencies (Raj et al. 2011, Kato et al. 2002, Ramprasad et al. 2004). In addition, RF absorption of Co particles can be utilised in cancer therapy (Xu et al. 2008, Aaltonen et al. 2004). This property may also be used for induction heating of similar composites (Miller et al. 2009).

Most conductive inks are composed of silver nanoparticles due to their excellent conductivity, typically 10^7 S/m (e.g. (Hsien-Hsueh et al. 2005). Low resistivity approaching that of bulk metals is desired for most printed electronics applications, such as antennas, optoelectronic devices, passive and active components, and device interconnects. However, in antistatic coatings for packaging, for example, higher surface resistivities in the range of 10^4 to 10^{11} Ω/□ are typical (ANSI ESD S541-2008). Material with this resistivity could also be applied for resistors and sensors (Gilleo 1996).

In nanoparticle form, silver costs about €7/g compared to €3/g for copper. Thus, copper would reduce costs but is, on the other hand, easily oxidised. The particles need to be in the nanoscale for inkjet printing, but inkjet is often preferred for the creation of fine structures. Larger particles will compromise printing quality due to the small dimensions of the inkjet nozzle. High conductivities for inkjet deposited copper patterns have so far been obtained for surfactant and polymer stabilised copper nanoparticles, as well as for copper nanoparticles encapsulated within a secondary metal, such as silver (Magdassi et al. 2010). In most cases, high temperature sintering and removal of the stabilising layer in an oxygen-free environment has been required to achieve line conductivities in the 10^6 -10^7 S/m range (approx. 10–20% of bulk copper) (Goo et al. 2010, Jeong et al. 2008, Park et al. 2007). Coating the copper particles with carbon protects the particles against oxidation and enables handling the ink in atmospheric conditions. These coated particles can afford an economical way to produce conductive inks, at least for the applications where lower conductivities are satisfactory. This was achieved in this thesis. A similar work has been published by Luechinger et al. (2008). A conductive ink was composed from carbon-coated copper nanoparticles produced in a flame spray.

An important application field for Co and Ni nanoparticles is biotechnology. In the field of nanobiotechnology, magnetic nanoparticles can be used for cancer therapy, cellular separation, and medical imaging (Roveimiab et al. 2012, Xu et al. 2008, Jun et al. 2008). For separation, receptors for cells or antibodies are attached to the magnetic nanoparticles. The particles are dispersed, the desired product attaches, and then the particles are collected with a magnet. Saturation magnetisation has to be high for collection of the particles. Smaller particles are more easily dispersed and enable a higher number of attachment structures per weight of the magnetic particle. The same properties are important in biological imaging and cancer therapy, where magnetic particles are injected into blood circulation. Biological receptors for, for example, tumours are attached to the particles and thus the particles are bound to the target site. Then imaging or therapy is performed using the magnetic properties of the particles. Afterwards, the particle can be separated from the blood stream using magnets.

The scattering of light can be electrically controlled using embedded metal nanoparticles (Müller et al. 2002). The optical radiation efficiency of copper is high (Tanabe 2007). The diameter of the particles has to be very precisely controlled for these applications and the size distribution has to be extremely narrow.

Catalytic applications for Co, Ni, and Cu nanoparticles include, for example, hydrogenation, oxygen reduction, water splitting, and synthesis of higher alcohols (Rodrigues 2002, Goubert-Renaudin and Wieckowski 2011, Chiang et al. 2011, Subramanian et al. 2009). In these applications, nanoparticles offer high specific surface areas and easier dispersion compared to catalysts with larger dimensions.

Copper nanoparticles are excellent sensors of carbohydrates (Wu et al. 2010, Xu et al. 2006, Male et al. 2004). Nickel nanoparticles are used for sensors of, for example, acetaminophen (Wang et al. 2007). For sensors, very small particles are used.

Comparatively, optoelectronics, sensors, and biotechnology applications require smaller numbers of particles than inks or magnetic materials. Thus, more expensive materials may be used for these applications.

1.4 Hydrogen reduction of metal chlorides

A gas-phase method for nanoparticle production has the potential for commercial success if it employs cheap precursors while achieving high particle mass concentrations and a high purity of the produced particles. Ideally, a selection of particle sizes can be made out of several metals. The method described below combines all these features.

In this thesis, a hydrogen reduction method is used to produce Co, Ni, and Cu particles from $CoCl_2$, $NiCl_2$, and CuCl. Gaseous metal chlorides are reduced to elemental metal at a high temperature by hydrogen gas, according to 7

$$MCl_x + \frac{x}{2}H_2 \rightarrow M + xHCl \tag{7}$$

Here, *M* is the metal. The saturation vapour pressures of metals and metal chlorides can be calculated with, for example, the FactSage program, which uses a widely validated database (GTT Technologies Gmbh). Figure 1.2 illustrates the saturation vapour pressures of cobalt, nickel, and copper chloride as a function of temperature.

The vapour pressures of Co, Ni, and Cu are very low, $2.2 \cdot 10^{-6}$, $2.4 \cdot 10^{-6}$ and $2.2 \cdot 10^{-3}$ Pa respectively, at the reaction temperature (950°C, FactSage). Since the saturation vapour pressure of the metal is several orders of magnitude lower than the saturation vapour pressure of the metal chloride, high particle number concentration is formed by nucleation as described below.

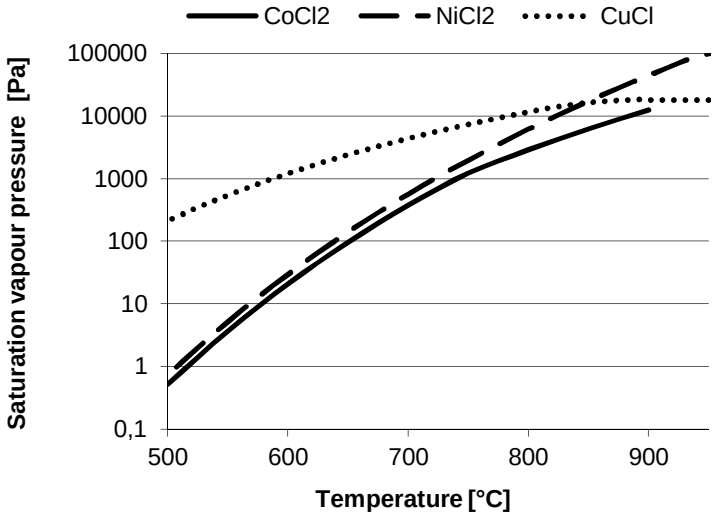

Figure 1.2. The saturation vapour pressures of $CoCl_2$, $NiCl_2$, and CuCl.

Using Co formation as an example, the formation rate of Co is:

$$\frac{d[Co]}{dt} = k_1'[CoCl2][H2] \tag{8}$$

Here, *[Co]* is the concentration of Co molecules per cubic metre, k_1' is the reaction rate constant for Co formation, and *[CoCl2]* and *[H2]* are the $CoCl_2$ and H_2 concentrations. The H_2 concentration is 13.8 mol-% (Paragraph 2) and even for maximum production rate, the H_2 concentration is never decreased below 13.3 mol-%. For the purpose of understanding the particle formation process, *[H2]* can be assumed to be constant and $k_1 = k_1' \cdot [H2]$.

At the same time, the opposite reaction also occurs:

$$\frac{d[CoCl2]}{dt} = k_2[Co][HCl] \tag{9}$$

In this case, *[HCl*] cannot be assumed to be constant. The Co inside the particle is not available for this reaction. Thus, the atomic concentration of cobalt molecules available for reaction to chloride, *[Co],* is sum of the gas-phase and the surface Co atoms.

Jang et al. (2003) measured the kinetics of $CoCl_2$ reduction and Suh et al. (2005) the kinetics of $NiCl_2$ reduction. They used only the Co formation reaction and assumed *[H2]* to be constant. The Co formation rate is equal to the decrease of $CoCl_2$. Then, Equation (8) can be integrated for estimation of reaction constant k_1:

$$k_1 = -\frac{\ln {}^{[CoCl2]}/_{[CoCl2]_0}}{t} \quad (10)$$

The kinetic constant may also be expressed through the Arrhenius formula:

$$k_1 = A \exp\left(\frac{-E_a}{RT}\right),$$

Here, *A* is the pre-exponential factor, E_a activation energy, *R* gas constant, *T* temperature, *t* time, and sub-index *0* indicates initial concentration. Jang et al. (2003) and Suh et al. (2005) obtained E_a of 110.27 and 103.79 kJ/mol for Co and Ni, respectively. The pre-exponential factors were $1.50 \cdot 10^7$ (Co) and $7.34 \cdot 10^6$ 1/min (Ni). These values result in k_1 = 293 and 271 1/min for Co and Ni, respectively, at 950°C.

The reduction of CuCl by hydrogen is widely studied in the 300–500 °C range (Gelatos et al. 1993, Kekesi et al. 1995, Serban et al. 2004). A high-temperature kinetic study exists of the reverse reaction of CuCl and H_2 production from Cu and HCl (Goubert-Renaudin 2011). The low-temperature studies give an activation energy of 110–140 kJ/mol for the CuCl reduction and half of that for the reverse reaction. The high-temperature study gives 68 kJ/mol for the reverse reaction (the same as for lower temperatures), indicating that 130–140 kJ/mol is correct also around 900°C. In addition, experiments show that CuCl is actually a trimer, $(CuCl)_3$, in the gas phase (Brewer, Lofgren 1950).

In the early works about metal chloride reduction in the gas phase (Dugleux, De Almeida Marques 1980), significant accumulation of metal on the reactor walls was observed. The authors explained this as due to selective surface reaction of the metal chlorides. Accounting for the surface reaction, the total reaction can be modelled through:

$$\frac{d[CoCl2]}{dt} = \quad (12)$$

$$-k_1'[CoCl2][H2] - k_3[CoCl2][Co_s][H2] + k_2[Co_g][HCl] + k_2[Co_s][HCl]$$

where k_3 is the surface reaction constant, $[Co_s]$ is the concentration of surface Co atoms ($1/m^3$), and $[Co_g]$ the concentration of gas phase cobalt atoms. A rough estimate of the number of surface atoms $n_{Co,s}$ per spherical particle of diameter *d* is given by:

$$n_{Co,s} = \frac{4\pi\left(\frac{d}{2}\right)^2}{(2r_{Co})^2} \quad (13)$$

Then $[Co_s] = c_n \cdot n_{co,s}$, where c_n is the particle number concentration ($1/m^3$). The atomic radius r_{Co} of Co is 125 pm. The prefactor ½ is used to estimate the decreased probability of surface atoms colliding with gas-phase atoms compared to gas-phase atoms, as roughly half of the atom surface is towards the particle surface.

The metal vapour that forms in the reduction reaction forms new particles by nucleation. The process is driven by supersaturation, the amount of metal vapour that exceeds the saturation concentration at the temperature. The Kelvin ratio (Friedlander 2000) gives the critical radius d^* for a stable liquid particle at a given supersaturation $S = p/p_s$:

$$\ln\frac{p}{p_s} = \frac{4\gamma M}{\rho R T d^*} \quad (14)$$

Here, γ is surface tension, M molar weight, and ρ density. For a solid particle, the formula has to include the different surface free energies of all the crystal faces of the particle of an equilibrium shape and the corresponding distances from a defined centre of origin. However, in a rapid particle formation process, such as in this thesis, the shape of the forming particles is not very likely to be the equilibrium shape.

The nucleation of particles is a challenging computational task and classical theories do not match experiments very well. In addition, the nucleated particles grow by condensation, surface reaction, and collisions with other particles. These complicated phenomena are not discussed here. The topic is covered, for example, by Pyykönen (2001) and Büsser (2011). An important thing is, however, the sintering timescale. Palasantzas et al. (2006) found that for 15 nm Co particles, the sintering time scale at the temperature of the reaction region of this thesis is about 40 s (Palasantzas, et al. 2006). For larger particles, the relevant sintering time is longer.

The melting point of a nanoparticle T_m is decreased from the bulk melting point $T_{m,bulk}$ according to (Friedlander 2000):

$$T_m = T_{m,bulk}\left(1 - \frac{4\sigma}{H_f \rho d}\right) \quad (15)$$

Here, σ is the solid-liquid interface energy and H_f the heat of fusion. Table 1-1 gives the basic physical properties of Co, Ni, and Cu and the maximum diameter for a liquid particle at 950°C, calculated with Equation 15 as well as the saturation ratio for a stable 1 nm particle, calculated with Equation 14. This saturation ratio is very dependent on the surface tension of the particle, which is affected by the

composition of the gas phase and the adsorption of gases on the particle surface (Gallois and Lupis 1981). Therefore, it should be considered a very rough estimate.

When a particle grows by condensation, there is a heat flux on the particle due to condensation of the metal vapour. This could increase the particle temperature clearly above the temperature of the surrounding gas. However, when the reaction temperature is high, such as in this thesis, radiation is the dominant form of heat transfer. Then, the temperature of the particle does not increase much above the reaction temperature, even if the particle grows by condensation and the vaporisation heat flux is significant. Therefore, these effects can be neglected here. A detailed order of magnitude calculation is shown in Appendix A.

Table 1-1. The bulk melting ($T_{m,bulk}$) and boiling temperature ($T_{b,bulk}$), density (ρ), heat of fusion (H_f) , surface tension (σ), and solid-liquid surface energy (γ) (Zeng-yun et al. 2002) for bulk Co, Ni, and Cu. In addition, the maximum diameter of a liquid particle at 950°C (d_{950}), and the saturation ratio for a stable 1 nm particle are shown. The maximum diameter is computed using Equation 15. The surface tensions are obtained from Brillo, (2005) and Yao (2002).

	Co	**Ni**	**Cu**
$T_{m,bulk}$, °C	1495	1455	1083
$T_{b,bulk}$, °C	2870	2730	2570
M, g/mol	58.93	58.69	63.55
ρ, kg/m^3	8890	8900	8960
H_f, kJ/kg	280	310	205
σ, J/m^2	0.293	0.382	0.256
γ, N/m	1.7	1.6	1.3
d_{950}, nm	1.5	1.9	5.7
p/p_s for $d^* = 1nm$	90	70	40

1.4.1 Carbon coating

Ethene (C_2H_4) decomposes to methane (CH_4), ethane (C_2H_6), and carbon (C) at high temperatures (700–950°C). The detailed decomposition pathways are studied, for example, by Jensen et al. (1994) and are relatively complex. The decomposition of ethene is catalysed by the metal nanoparticles and further increased by the presence of hydrogen and chlorine (Chambers 1997). Cobalt catalyses ethene decomposition at a faster rate than nickel (Narkiewicz et al. 2010). Because the reaction is catalysed by the metal nanoparticles, the reaction rate cannot be calculated using a similar equation to Equation 12. It will be shown in Chapter 3.3 that the conversion of ethene to carbon is not linearly dependent on ethene concentration.

1.4.2 Formation of CNT-like structures

Copper particles are not usually considered the best candidates for nanotube growth (Nasibulin et al. 2003). Zhou et al. (2006) showed, however, that copper particles can be very effective catalysers for nanotube formation in conditions very similar to those used in this thesis. Törndahl et al. (2004) studied copper layer formation in CVD from CuCl with and without water addition. They found that the combined reaction rate of CuCl to Cu is faster with water, when the reaction proceeds through two steps:

$$2CuCl + H_2O \rightarrow Cu_2O + 2HCl \quad (16)$$

$$Cu_2O + H_2 \rightarrow 2Cu + 2H_2O \quad (17)$$

A faster reaction rate gives a longer residence time for nanotube formation with the catalysts particles available. In addition, water is known to increase formation of carbon nanotubes through cleaning of the surface from graphitic and amorphous carbon (Nasibulin et al. 2006).

2. Experimental methods

2.1 Co, Ni, and Cu nanoparticle production by hydrogen reduction

The experimental setup was a single piece quartz reactor, as illustrated in Figure 2.1. Precursor powder was fed by a powder feeder to a heated evaporation column composed of porous alumina pellets. The stack temperature was 600–850°C. The evaporated precursor was carried along a nitrogen gas flow to a reaction zone. The use of the evaporation column maximises the evaporation area if the precursors are liquid. The melting points of $CoCl_2$, $NiCl_2$, and CuCl are 735, 1001, and 426°C. The saturation vapour pressures of the precursors are high at the chosen evaporation temperatures, as seen in Figure 1.2. Thus, high mass concentrations of the produced metal nanoparticles are possible for the setup.

In the reaction zone, hydrogen gas was fed into the metal chloride – nitrogen mixture at 900–950°C. The flow was then quenched with room temperature nitrogen gas. Particles were collected in PTFE filter bags. After filtering the particles, the gas flow was cleaned. First it was bubbled through neutralisation tanks filled with NaOH solution to remove HCl. Then the gas flow was dried with a diffusion dryer and filtered for NaCl particles. The gas flows were controlled with mass flow controllers before the furnace and a pump was placed after the cleaning of the gas. This pump compensates for the pressure loss at filters and neutralisation tanks, enabling operation of the furnace within 2 kPa of ambient pressure.

The production costs of the metal nanoparticles produced by hydrogen reduction mainly consist of precursor chloride, hydrogen, nitrogen, and heating. The costs of facility and personnel are heavily dependent on the amount produced and cannot be realistically estimated here. In an industrial facility, the dilution nitrogen could be recycled. The bulk price of $CoCl_2$ is about $10 per kg or roughly €0.02 per gram of Co. The nitrogen price can be estimated to be €1/m^3. For particle mass concentration of 20 g/m^3 (prior to dilution, see Table 3-1), the total gas consumption is 0.4 m^3/g. Then the nitrogen price is €0.4 for 1 g of particles if the dilution gases are not recycled. Hydrogen costs are roughly the same as nitrogen and are included in the 0.4 m^3/g. Thus precursors and gases together total roughly €0.4/g.

The current price of electricity is about €40/MWh in Finland. The heat capacity of nitrogen, $c_{p,N2}$, is 1.1 kJ/kg·K (average for the 20–950°C range). At NTP, the density of nitrogen is 1.15 kg/m^3. Thus, for 1 g of particles, the nitrogen weighs $m = \rho \cdot V = 0.44$ kg N_2/g Co. The efficiency of heating, E, is estimated to be 0.5. Then cost of energy is $p_e = m \cdot \Delta T \cdot c_{p,N2}/E =$ €0.01/g of Co. Altogether, it is clear that in terms of raw materials and energy, the price of the produced metal nanoparticles is competitive with the hydrogen reduction method.

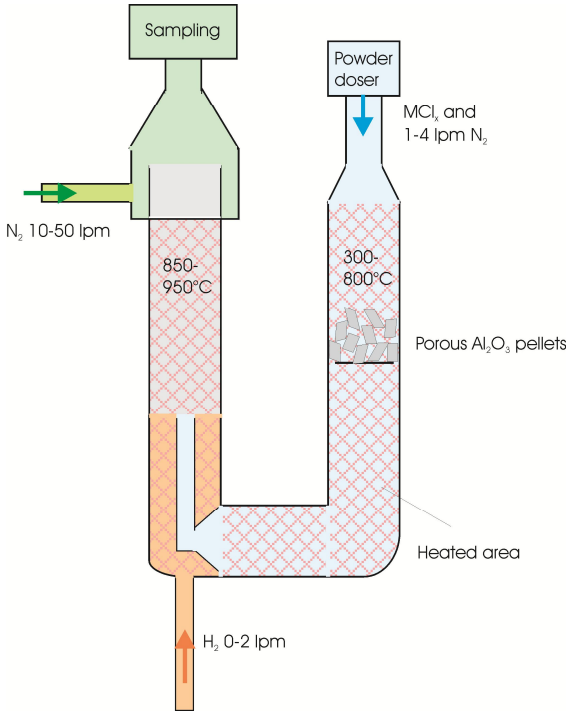

Figure 2.1. The quartz furnace for producing Co, Ni, and Cu nanoparticles with the hydrogen reduction method.

2.1.1 Carbon coating and CNT formation

Metal nanoparticles were coated by feeding ethene-nitrogen mixture into the reaction zone together with hydrogen. In the carbon-coating experiments, the evaporation temperature was always 800°C and the reaction temperature 950°C. Ethene (C_2H_4) decomposes to methane (CH_4), ethane (C_2H_6), and carbon (C) in the reaction zone. The reaction is incomplete and more than 50 mol-% of the ethene remains unreacted. The metal surface catalyses the decomposition reaction and a carbon layer forms on the metal nanoparticles. This suppresses further growth of the metal nanoparticles and can be used to control the number average diameter of the core particles. The carbon-coated particles are referred to as Co+C, Ni+C, and Cu+C.

The growth of carbon nanotube-like structures was promoted by adding water to the reaction zone together with ethene. A nitrogen flow was bubbled through a bottle of de-ionised water before feeding into the reaction zone. The CNT growth was experimented with copper particles. These particles are referred to as Cu+CNT.

The cost of ethene is similar to those of hydrogen and nitrogen in the large scale. Thus carbon coating does not significantly increase production costs of the particles.

2.1.2 Characterization methods

During particle production, the gas phase was analysed using Fourier-transform infrared spectroscopy (FTIR, Gasmet Dx4000) for HCl, H_2O, CO, and CO_2. HCl concentration is a direct measure of the reaction rate of the metal chloride (Equation 7). The other compounds were followed to ensure the safety and quality of the process. If ethene was fed into the reactor, CH_4, C_2H_4, and C_2H_6 concentrations were also measured to observe the degree of ethene degradation.

Membrane filter samples were taken from the gas flow during an experiment (Millipore 0.2 μm FG Fluoropore, flow rate 0.38 Nlpm). These filters were weighed, which gives a second measure of the mass concentration of the produced particles. The particles collected on these filters were imaged with transmission electron microscopy (FE-TEM, Philips CM-200 FEG equipped with EDS analyser). The number average diameter of the primary particles (NAD) was determined by measuring the diameter of 150–500 particles from these micrographs. Sample standard deviation (SD) and specific surface area (SSA) were determined directly from these data points. The SSA was also measured directly using the Brunauer-Emmet-Teller method (BET). In addition, the crystal structure of the particles was studied with selected area electron diffraction (SAED).

All gas and mass concentrations are given at NTP. Mass concentrations are given as prior to dilution concentrations for easier comparison to other relevant methods. Ethene concentrations are always given as the concentration in the reaction zone prior to reaction and dilution.

The structure was also characterised with x-ray diffraction (XRD, Philips X'pert MPD x-ray diffractometer) and elemental composition with x-ray fluorescence (XRF, Philips PW2404 x-ray spectrometer with SemiQ). The XRF method does not directly see carbon and thus cannot be used to determine small carbon concentrations. The oxidation behaviour of particles is analysed with thermogravimetric analysis (TGA). Assuming full oxidation to Co_3O_4, the analysis was also used to estimate the carbon content of the carbon-coated Co and Cu particles.

Saturation magnetisation M_s, coercive field H_S, and remnant magnetisation M_r were measured using a Quantum Design SQUID magnetometer with a 7 T superconducting magnet at Aalto University, by Prof. Sebastiaan van Dijken. Measurements were conducted at room temperature (300K) within one day after production of Co+C particles. The M_s was normalised to the Co weight. Samples for magnetic measurements were taken from filter bags and from membrane filters.

3. Results and discussion

3.1 Co, Ni, and Cu particles

In the Co production experiments (Publication I), it was observed that the particle mass concentration for an 800°C evaporation temperature is 56% of the theoretical maximum particle mass concentration (50 g/m^3 in the reaction zone), calculated from the saturation vapour pressure of $CoCl_2$. This is an excellent result for continuous powder feeding. For Ni, only 20% of the theoretical maximum was reached because nickel chloride does not melt in the evaporation column. For copper, only 3% of the theoretical maximum was reached. In this case, the powder feeding rate limits the evaporation rate.

The primary particle size was 84 nm for Co at an evaporation temperature of 800°C. The particles were spherical, as illustrated in Figure 3.1. The Ni particles were smaller and faceted. The maximum diameters for liquid particles in Table 1-1 show that the particles that were produced in this thesis are much larger than the diameter of liquid particles at the reaction temperature. Thus, the spherical shape of the particles cannot be formed by collisions of liquid particles fusing together. Larger particles colliding would be seen as separate primary particles, as the characteristic sintering time is tens of seconds (see Chapter 1) – a very long time scale compared to a <1 s reaction time. The primary particle size seen in the TEM images is thus the result of growth by condensation and surface reaction.

The reaction rates and vapour pressures are very similar for Co and Ni. The average primary particle diameter is similar for the same mass concentration, but the Co particles are spherical compared to faceted Ni particles. The faceting of Ni nanoparticles has been investigated by molecular dynamic by Karâkina et al. (2010), but the definitive reason for the difference from Co is not known.

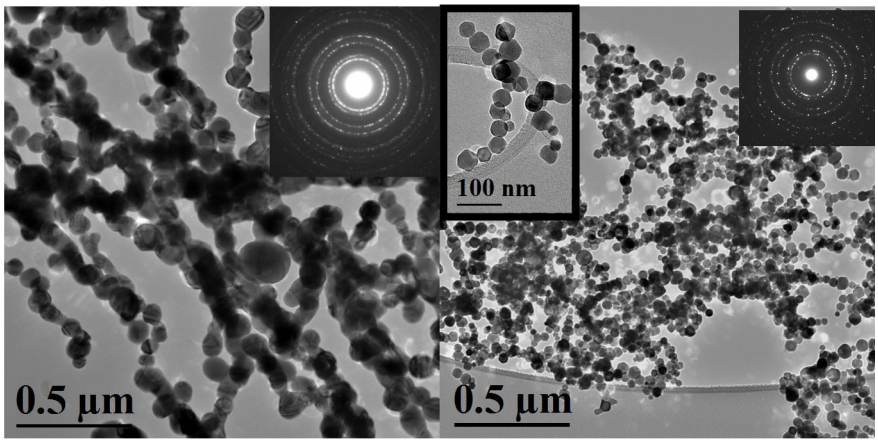

Figure 3.1. Left: Co particles with an evaporation temperature of 800°C and a reaction temperature of 900°C. Right: TEM image of Ni particles. The top right corner inserts show electron diffraction patterns for Co and Ni. The higher magnification insert for Ni shows faceting not seen in Co or Cu particles in this thesis.

Figure 3.3 (p. 33) illustrates the XRD graph of Co particles with 84 nm NAD. The particles show an FCC structure, which is also confirmed in the electron diffraction analysis. The diffraction pattern is shown as an insert in Figure 3.1. The equilibrium crystal structure for cobalt is HCP at room temperature. FCC is the equilibrium phase formed at 450°C. However, FCC cobalt is stable at room temperature. The formation of a high-temperature crystal structure is a significant difference between a low-temperature and a high-temperature manufacturing process such as this. No peaks were observed for $CoCl_2$ in this or other XRD graphs. The situation was the same for Ni and Cu; the XRD diffraction does not show unreacted metal chloride. The crystal structure is also FCC for Ni and Cu, but for these metals, it is the equilibrium phase at both room temperature and the reaction temperature. HCP Ni nanoparticles have been produced at intermediate temperatures (200–300°C) (Chen et al. 2007).

The size distribution of the particles was unimodal. The number average diameter of Co particles was 84 nm for particle mass concentration of 47 g/m^3 in the reaction flow. The standard deviation was 18 nm. Figure 3.2 illustrates the size distribution for this sample. The NAD was dependent on the particle mass concentration. For 0.2 g/m^3 and below, the NAD was about 20 nm.

Table 3-1. The NAD and particle mass concentration c_m for Co, Ni, and Cu particles.

Material	NAD nm	c_m g/m^3
Co	20	0.5
Co	84	47
Ni	60	19
Cu	121	20

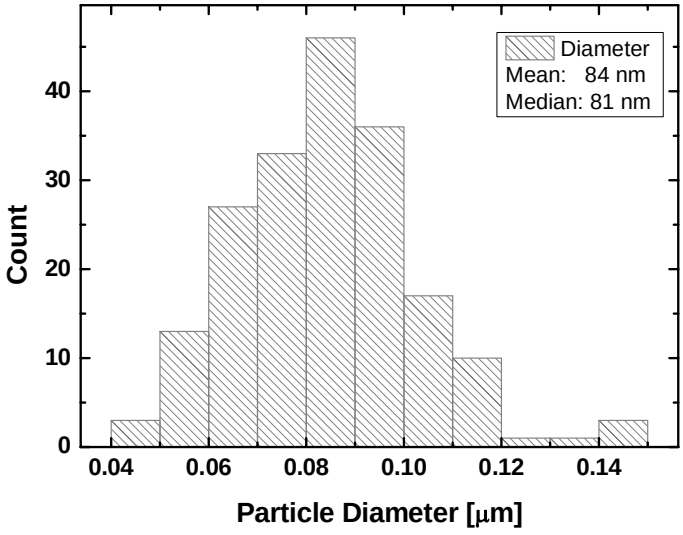

Figure 3.2. Size distribution of Co particles (Publication I). The evaporation temperature was 800°C and the reaction temperature 900°C. The standard deviation was 18 nm.

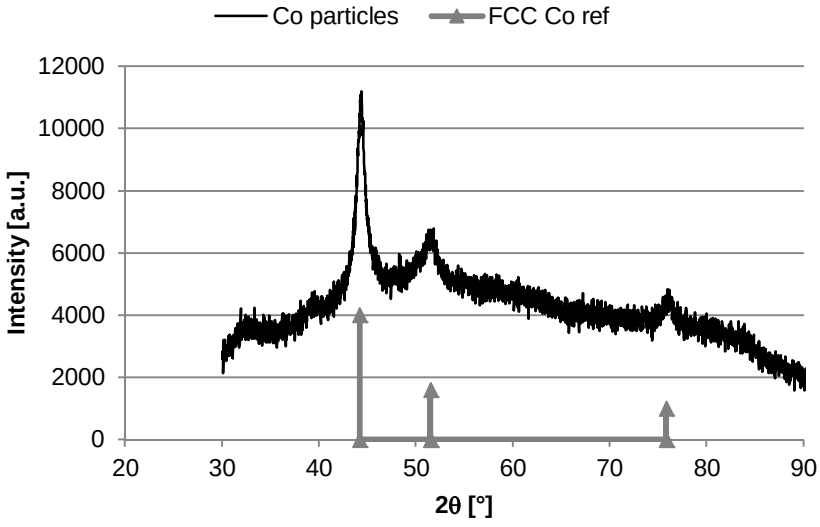

Figure 3.3. XRD of Co particles with 84 nm NAD. The crystal structure corresponds to FCC Co.

A typical XRF result is shown in Table 3-2. The analysis was performed on Co particles for an experiment with mass concentration 28 g/m^3. The main impurity was Cl. After the XRF analysis, the sample was purged with nitrogen at 200°C for 30 minutes. The chlorine content was decreased from 0.9 wt-% to 0.45 wt.-% after the purging. The other elements were not affected. The vapour pressure of $CoCl_2$ is $4.2 \cdot 10^{-10}$ Pa (FactSage) at 200°C. If the nitrogen flow was saturated with $CoCl_2$ during heating, the theoretical maximum evaporation, the evaporation of $CoCl_2$ would be $2 \cdot 10^{-7}$ g for a 1 g sample. This is much below the XRF accuracy. Thus, the decrease in Cl wt.-% cannot be due to $CoCl_2$ evaporation. The most likely reason is that there was HCl absorbed on the particle surfaces. The remaining 0.45 wt.-% chloride may be due to $CoCl_2$. The minimum conversion ratio is thus 0.9940 and more likely 0.9970.

Table 3-2. Typical XRF analysis result for Co particles. The reaction temperature was 900°C and the particle mass concentration 28 g/m3 in the reaction zone.

Element	wt.-%
Co	98
Cl	0.90
S	0.24
Ni	0.23
Na	0.15
Fe	0.02

3.2 Modelling results

A simplified calculation model was constructed for Co to estimate the order of magnitude of k_1, k_2, and k_3. Equation 12 can be used to estimate the conversion of $CoCl_2$. The kinetics of mass transfer were neglected. As far as the model is considered, particle concentration stands for primary particle number concentration. The high primary particle concentration does lead to agglomeration and decrease in number concentration, but as the sintering time scale is very large compared to reaction time (see Chapter 1), these agglomerates are soft and do not affect the surface area available to gas phase reactions. Therefore, these agglomerates do not affect the calculation and may be ignored. They may have a significant effect on the behaviour of the particles in applications, though. Sintering of the particle does occur during the nucleation, when the particle size is close to the critical radius of a liquid particle, 1.5 nm for Co.

As the number concentration and diameter of the particles cannot be estimated with simple methods, the particle concentration was set to the final number concentration from the experimental results and Co vapour pressure to the saturation vapour pressure. For 80 nm Co particles with particle mass concentration c_m of 40 g/m^3, the particle number concentration c_n is $1.7 \cdot 10^{16}$ 1/m^3 at NTP, and assuming the particles are hard spheres, the number concentration c_n can be calculated with:

$$\frac{4}{3}\pi\left(\frac{d}{2}\right)^3 \rho c_n = c_m \tag{18}$$

The same equation was used during the evolution of the reaction to calculate the diameter of the particles. It was assumed that the particle number concentration is constant and that the particle mass concentration is equal to the Co formed by gas-phase and surface reactions. The gas-phase concentration of Co, $[Co]_g$, is low at saturation. The particle concentration, on the other hand, is high. Therefore, $[Co]_s$ is 4–6 orders of magnitude larger than $[Co]_g$. The hydrogen chloride concentration is calculated through conversion of $CoCl_2$: $[HCl] = 2([CoCl2]_0-[CoCl2])$. The $CoCl_2$ concentration is equal to surface Co atom concentration when conversion has reached 0.992.

The time step in the calculations was 1 ms. The initial particle diameter was set to 1 nm. This would roughly correspond to the first molecular clusters formed by nucleation. An initial concentration for gaseous Co molecules was also set; $[Co]_0 = 1 \cdot 10^{-30}$ Pa. The reaction temperature was set to 950°C. The corresponding reaction time in the setup used is 0.35 s, which was the end point of calculations. The initial cobalt chloride concentration $[CoCl2]_0$ was set to 923 Pa – the theoretical maximum for evaporation at 800°C (2 Nlpm evaporation flow over 6.5 Nlpm total reaction flow). The backward reaction rate k_2 is compared to k_1', thereby taking into account the hydrogen concentration. The H_2 concentration was 13.8 mol-% (or 13800 Pa) and it was assumed to be constant during the reaction. For comparison to the gas-phase reaction rate, a numerical value for the surface reaction rate, $k_3' = k_3 \cdot [Co_s]$, is also calculated for specific conditions.

The conversion of $CoCl_2$ as a function of various assumptions for k_1 and k_2, but neglecting the surface reaction *($k_3 = 0$)*, is illustrated in Figure 3.4. The value 300 1/min is that calculated from the E_A and A given by Jang et al.(2003) at 950°C. The resulting conversion is much lower than the experimental result in this thesis, even if the backward reaction did not exist. If a surface-specific reaction is not relevant, the conversion rate is in agreement with the experimental results of this thesis, when k_1 is 900 1/min or larger and k_2 between 0 and $0.5 \cdot k_1'$. The actual experimental conditions, such as losses and the details of the mixing of the reactant gases, are often attributed to observed reaction kinetics. Therefore, disagreement between the results observed with two different experimental setups is typical, and exact values should not be given without extensive experiments.

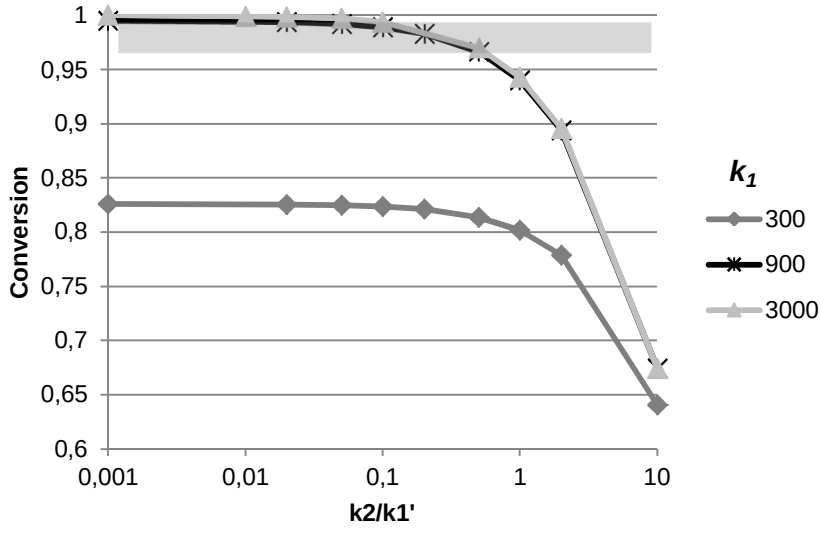

Figure 3.4. The conversion of $CoCl_2$ to Co as a function of parameters k_1 and k_2. In these calculations, surface reaction is not considered, $k_3 = 0$. The shaded area shows conversion from 0.97 to 0.995, which is the range that matches the experimental results, including measurement error and uncertainty in the HCl to $CoCl_2$ ratio in XRF results. The reaction time was 0.35 s.

The conversion of $CoCl_2$ to Co when taking the surface reaction in account is shown in Figures 3.5–3.8 (pp. 36–37). Now a higher reaction rate than earlier studies is still required if $k_3 = 1.2 \cdot 10^{-44}$ m^6/s or lower. At this value of k_3, the surface reaction is not very significant. When k_3 is $6.1 \cdot 10^{-44}$ or higher, on the other hand, k_1 and k_2 have a very small effect on the final conversion. Especially noteworthy is that then, as k_1 increases, the conversion decreases. As k_1 increases, the absolute value of k_2 increases for the same k_2/k_1' ratio. When the surface reaction is dominant, the final conversion is dominated by the backward reaction rather than the forward gas-phase reaction. In the

intermediate region, $1 \cdot 10^{-44} < k_3 < 6 \cdot 10^{-44}$ m^6/s, both the surface and gas-phase formation reactions for Co are relevant. The value of 300 1/min k_1 corresponds to $k_1' = 6.1 \cdot 10^{-24}$ m^3/s.

Figure 3.9 (p. 39) illustrates the proportion of surface reaction to gas-phase reaction, k_3'/k_1',' during the reaction for one value of backward reaction, $k_2 = 0.1 \cdot k_1'$. In addition, the conversion is shown on the right-hand side axis for the same parameter sets. When k_1 is 300 or lower, k_3' grows larger than k_1', while for higher k_1, the ratio stays below 1. The final conversions are almost equal, but when less than 0.1 s of reaction time has passed, there is a large variation in conversion. Thus, experiments with a very short reaction time would give more information on the reaction rate parameters.

Exact kinetic parameters cannot be obtained from the model, but some conclusions can be drawn. If surface reaction is not important, the reaction rate appears to be much higher than previously reported. If the surface reaction rate is about as important as the gas-phase reaction, the gas-phase reaction rate may be similar or faster than previously reported, but not lower. In addition, the backward reaction is slower than the forward reaction. If the surface reaction dominates, on the other hand, backward reaction may be even faster than the forward reaction, but nothing can be said of their absolute values. In the TEM images in Chapter 3.3, the carbon layer is always on top of the cobalt particles and cobalt layers are never observed on top of the carbon. If only the gas-phase reaction was relevant, condensation should be seen on at least some carbon surfaces. Even though two experimental processes may give conflicting results, it is not very likely that the surface reaction has no role. However, further experiments are required to verify this.

The kinetics of mixing may have a large effect on the observed conversion ratio and should be taken into account before exact numbers are given for the reaction rate constants. If the conversion involved only limited mixing, the reduction rate of $CoCl_2$, $NiCl_2$, and CuCl would be about the same, resulting in primary particles of the same size for a given mass concentration. The difference in Co and Ni particle size in Table 3-1 (p. 32) can be explained by a difference in particle mass concentration. However, Cu particles grow much larger than Co particles even for lower particle mass concentrations. The high-temperature studies that were referred to in Chapter 1 indicate a higher backward reaction rate for CuCl. This would decrease the nucleation rate, as a smaller gas-phase concentration of Cu would exist. The existing particles could grow larger by surface reaction and condensation growth. The purity of the Cu particles requires a significant proportion of the surface reaction if a large proportion of backward reaction exists. The best fit to this and earlier studies is that there is a small proportion of backward reaction for Co and a larger one for Cu, and that a significant fraction of the metal is formed by surface reaction. The formation process is graphically illustrated in Figure 3.10 (p. 39).

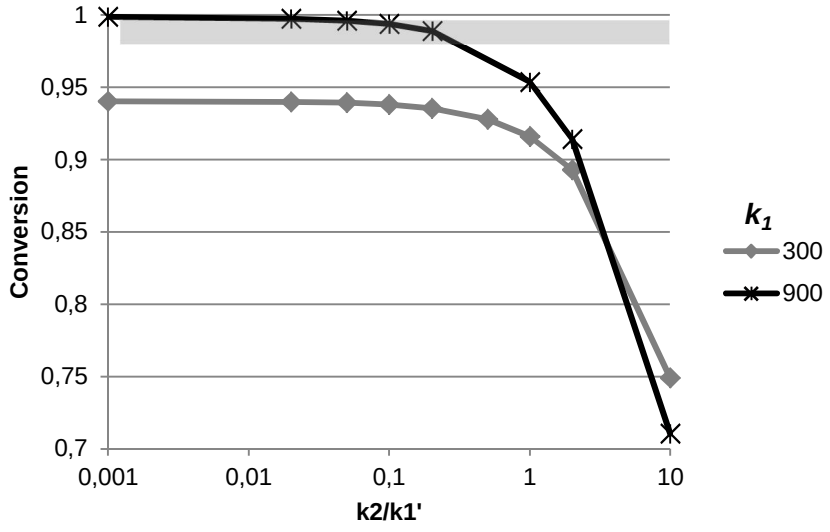

Figure 3.5. Conversion of $CoCl_2$ to Co when $k_3 = 1.2 \cdot 10^{-44}$ m^6/s. The shaded area shows conversion between 0.98 and 0.995, which is the range that matches the experimental results including measurement error and uncertainty in the HCl to $CoCl_2$ ratio in XRF results. The reaction time was 0.35 s.

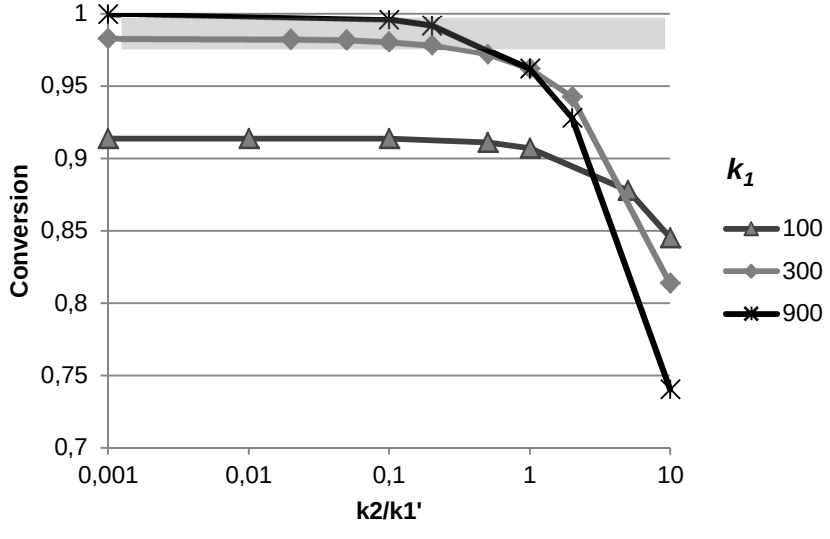

Figure 3.6. Conversion of $CoCl_2$ to Co when $k_3 = 2.5 \cdot 10^{-44}$ m^6/s. The shaded area shows conversion between 0.98 and 0.995, which is the range that matches the experimental results, including measurement error and uncertainty in the HCl to $CoCl_2$ ratio in XRF results. The reaction time was 0.35 s.

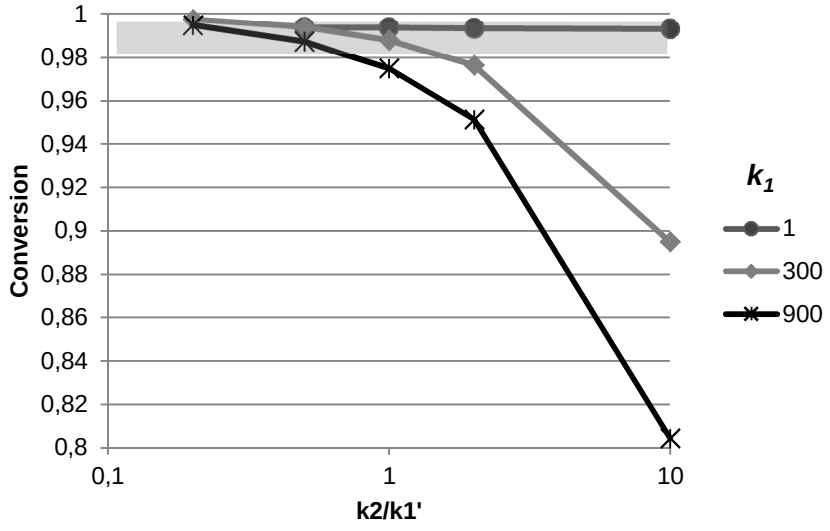

Figure 3.7. Conversion of $CoCl_2$ to Co when $k_3 = 6.1 \cdot 10^{-44}$ m^6/s. The shaded area shows conversion between 0.98 to 0.995 which is the range that matches experimental results including measurement error and uncertainty in the HCl to $CoCl_2$ ratio in XRF results. The reaction time was 0.35 s.

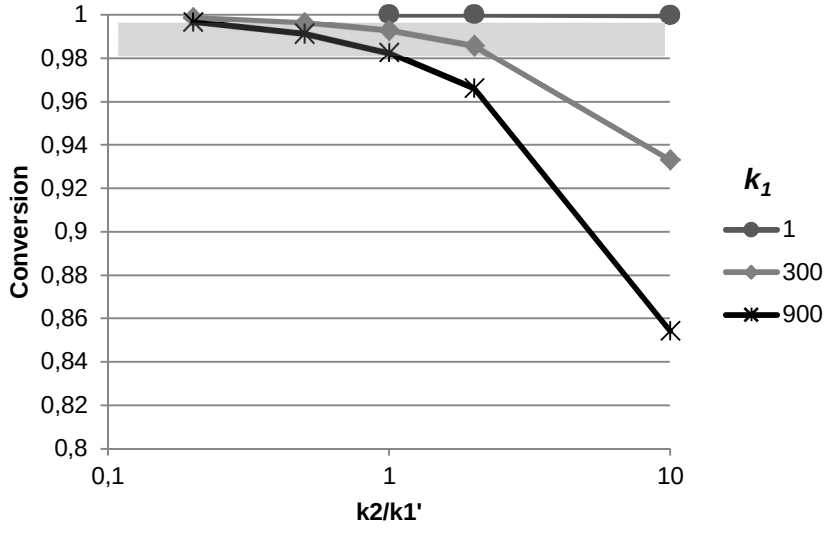

Figure 3.8. Conversion of $CoCl_2$ to Co when $k_3 = 1.1 \cdot 10^{-43}$ m^6/s. The shaded area shows conversion between 0.98 and 0.995, which is the range that matches the experimental results, including measurement error and uncertainty in the HCl to $CoCl_2$ ratio in XRF results. The reaction time was 0.35 s.

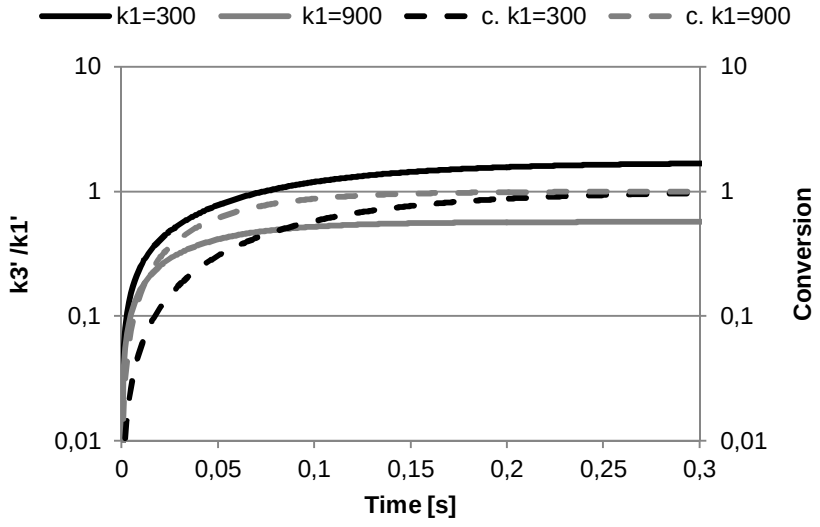

Figure 3.9. The ratio of k_3'/k_1' during the reaction is shown by the solid lines on the left-hand axis. In addition, the dashed lines show the conversion (c.) as a function of time on the right-hand side axis for the same cases. In these calculations, $k_2 = 0.1 \cdot k_1'$ and $k_3 = 2.510^{-44}$ m^6/s.

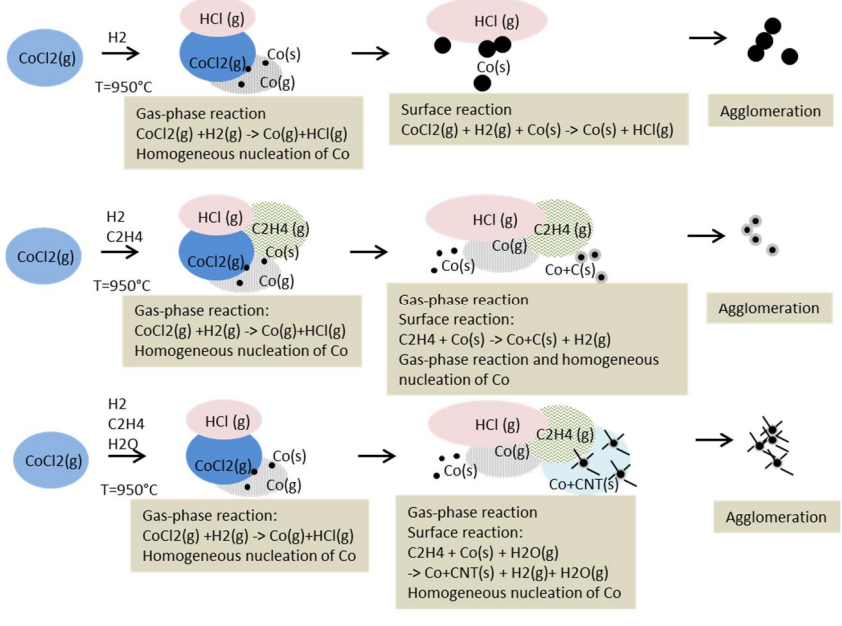

Figure 3.10. The formation of pure metal particles, carbon-coated particles, and CNT-coated particles.

3.3 Carbon-coated Co and Cu particles

When ethene was fed into the reactor, the particles were covered with a graphitic layer (Publications II, III and IV). This is seen in Figure 3.13 and Figure 3.14 (p. 42). In the TEM micrographs, carbon always covered the particles. Condensation or reaction of the metal on the carbon surface did not occur. This strengthens the conclusion that the metal surface reaction dominates the core particle growth process.

The growth rate of the particles decreases when ethene concentration increases. When ethene concentration is increased, the number average primary particle size decreases. This is illustrated in Figure 3.11. Without ethene, the particle size distribution was unimodal irrespective of particle size or material (Co, Ni or Cu). With ethene, the distribution was unimodal with low (<0.1 mol-%) and very large (>1 mol-%) concentrations. In the intermediate range, 0.1–1 mol-%, the size distribution was bi-modal, as illustrated in Figure 3.12. The first mode coincides with the peak in the high-ethene concentration experiments.

Co, Ni, and Cu nanoparticles are known to catalyse carbon formation in the <10 nm size range. Then there are two competing reactions at the particle surface: metal chloride reduction and ethene decomposition. Ethene concentration is equal to initial cobalt chloride concentration for 0.92 mol-% C_2H_4 in the reaction flow.

In the <0.1 mol-% ethene case, the surface reaction of the metal chloride dominates the core particle growth process. In the intermediate region, where the ethene concentration is 0.1–1 mol-% of the total reaction flow, both reactions are important and hence the bimodal distribution is observed. For the largest ethene concentrations, the carbon formation dominates and very small particles are formed. The primary particle number concentration is higher compared to the same particle mass concentration of metal without coating. As the particles that are covered with carbon cease to grow by surface reactions, gas-phase reaction leads to nucleation of new particles. The detailed process is likely to be affected by diffusion of ethene intoto the metal chloride – nitrogen flow.

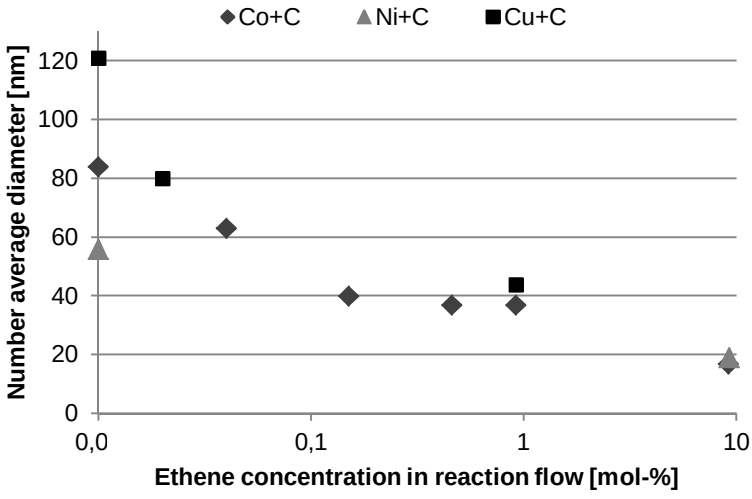

Figure 3.11. The effect of the ethene concentration on the number average particle diameter.

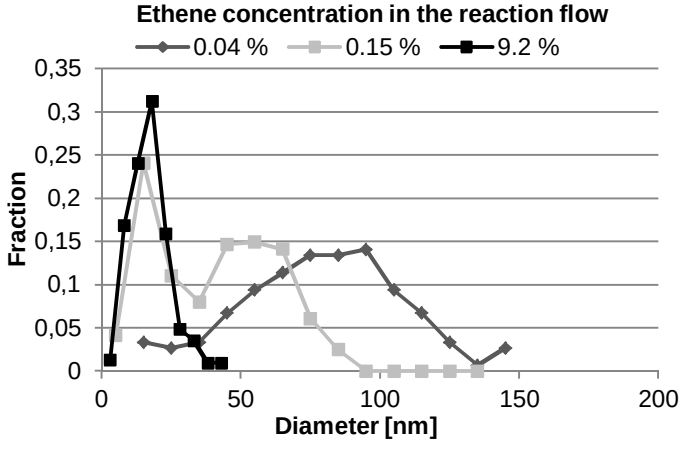

Figure 3.12. Size distribution of Co+C particles produced with 0.04, 0.15, and 9.2 mol-% ethene in the reaction flow. The size distribution is clearly bimodal for the 0.15 mol-% ethene case and unimodal for the other ethene concentrations.

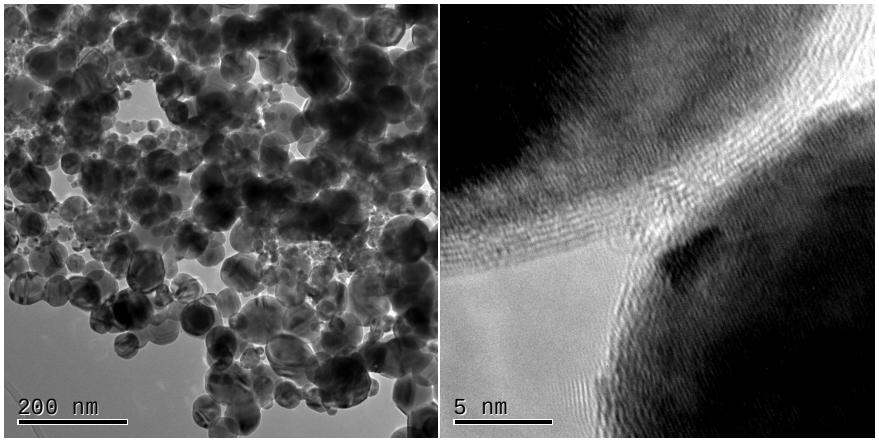

Figure 3.13. TEM images of Co+C particles with 40 nm NAD. The graphitic carbon layers are clearly visible on the right-hand side image.

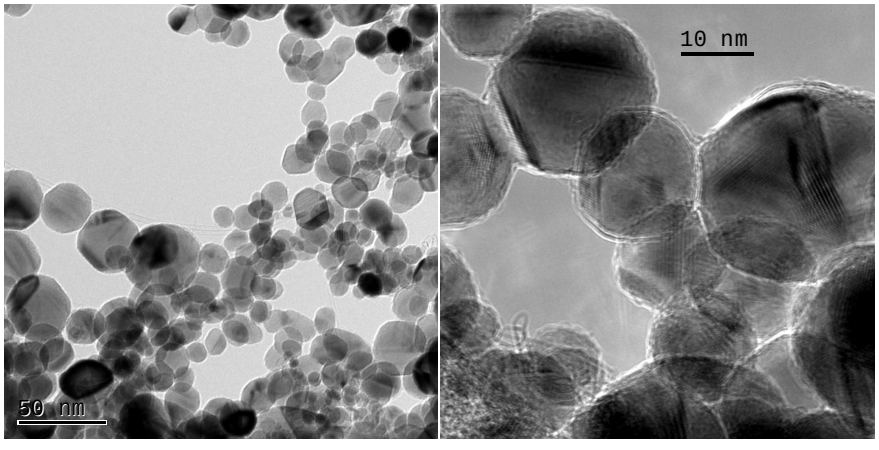

Figure 3.14. TEM image of Co+C particles with 17 nm NAD.

Table 3-3 gives the standard deviations and specific surface areas for Co+C particles. It is important to note that the specific surface areas derived from TEM micrographs are almost equal to those measured by the BET method. This indicates that the particle size distribution acquired through TEM analysis is representative. The carbon-coating layer is clearly visible in the TEM images, Figure 3.13 and Figure 3.14. The match between TEM and BET SSAs also confirms that the graphitic smooth surface seen in TEM is a good representation of the particle surface. An amorphous carbon layer is not smooth and would give a much higher BET surface area. The XRD grain size is also quite close to the TEM derived average primary particle diameter. The XRD graph is seen in Figure 3.15. There, FCC Co

and Cu were observed for Co+C and Cu+C particles similarly to pure metals. Unreacted metal precursor was not found.

Table 3-3. The determined properties of Co and Co+C particles for ethene concentrations 0–9.2 mol-% in the reaction flow.

Ethene	c_m	NAD (TEM)	SD (TEM)	Crystal size (XRD)	SSA (BET)	SSA (TEM)
mol-%	g/m^3	nm	nm	nm	m^2/g	m^2/g
0	10	84	17		7	8
0.04	13	63	37		10	11
0.15	14	40	22	35	11	11
9.2	10	17	7	23	25	29

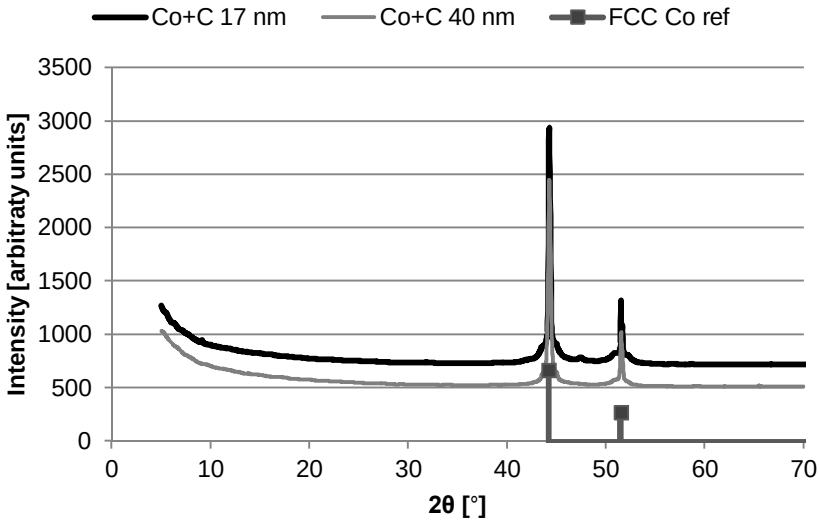

Figure 3.15. The XRD graph of Co+C particles with 17 and 40 nm NAD.

The carbon content of the Co+C and Cu+C particles depended on the ethene concentration, as seen in Table 3-4. Higher ethene concentration increased the carbon concentration of the particles. However, the carbon wt.-% of the particle mass only doubles when the ethene concentration is increased by two orders of magnitude. The conversion of ethene to carbon is thus not linearly dependent on the ethene concentration.

The carbon concentrations are higher for the copper particles than for the corresponding Co+C particles. The degradation of ethene is catalysed to a greater extent by the copper particles. For Cu+C, the carbon detected by XRF is higher than that analysed with TGA. Most likely, some of the carbon formed carbon diox-

ide in TGA already during the oxidation of the metal, and thus the final weight loss underestimates the carbon content of the samples. Therefore, it is likely that the XRF-analysed carbon concentration is closer to the actual carbon concentration.

The ethene conversion is also estimated in Table 3-4. The calculation is based on the carbon found in the particles by TGA, ethene fed to the reactor, and total particle mass concentration. This calculation should be considered only a rough estimate. However, it is seen that the relative ethene conversion decreases as the ethene concentration increases. The conversion is also much higher for Cu than for Co. For 44 nm Cu, the thickness of the carbon shell would have to be 4.5 nm to obtain the 16 wt.-% carbon. This is not likely to be obtained through a thin graphitic coating.

Table 3-4. The carbon content and ethene conversion of Co+C and Cu+C particles as a function of the ethene concentration. In the Cu+C experiments, the mass concentration was 20 g/m^3.

	Co+C				Cu+C			
C_2H_4 mol-%	NAD nm	C, wt.-% XRF	C, wt.-% TGA	C_2H_4 conversion %	NAD nm	C, wt.-% %	C, wt.-% TGA	C_2H_4 conversion %
0	84	0	0		121	0	0	
0.05					88		3.1	93
0.15	40		3	19				
0.92					44	16	11	45
9.2	17		6.2	0.63				

In Figure 3.16, the TGA curves are given for two Cu+C samples. Without ethene coating, copper nanoparticles form oxide at room temperature. The carbon layer on the particles increases the oxidation initiation temperature to 114°C. The oxidation initiation occurs at the same temperature for both carbon concentrations, but for the 0.05 mol-% ethene in the reaction flow, the oxidation is immediately fast, whereas for 0.92 mol-% ethene in the reaction flow, the oxidation is first slow and the oxidation rate increases at 170°C. For pure Co particles, the oxidation initiation temperature is 165°C. This is already a great oxidation resistance for metal nanoparticles. With carbon coating, it is elevated to 185–202°C, depending on the ethene concentration.

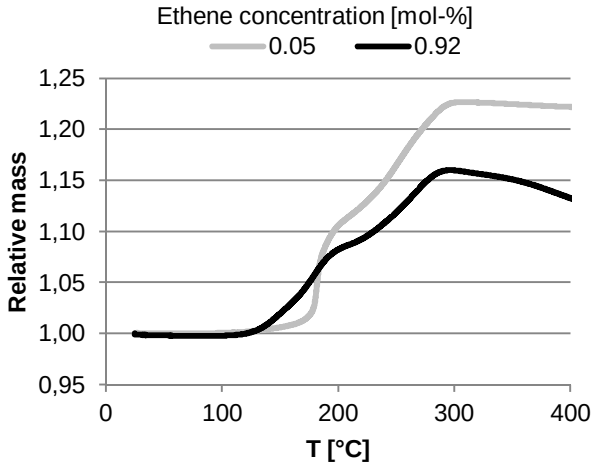

Figure 3.16. TGA curves for Cu+C particles with two ethene concentrations.

3.4 Formation of carbon nanotube-like structures

In general, the ethene decomposition leads to the formation of a graphitic shell on the cobalt and copper core particles. Ethene is used in CNT production in very similar reaction conditions, as explained in Chapter 1.4. However, the particles quickly grow larger than the preferred CNT catalyst particle size (~3–10 nm). The metal particle mass concentration is also much higher than in CNT production. However, with water addition, significant amounts of CNTs were formed, as seen in Figure 3.18 (Publication IV).

The size distributions of Cu, Cu+C. and Cu+CNT particles are shown in Figure 3.17. The size of the Cu+CNT particles is slightly larger than that of the Cu+C particles with the same ethene concentration in the reaction flow. This is likely due to the cleaning of the carbon surface and the preference to form carbon in the tubes rather than on the particle surface. XRF indicated 9 wt.-% of carbon in the powder, smaller than the carbon content of the Cu+C particles (16 wt.-%). This is also likely due to the cleaning of the carbon surface by water.

The BET surface area of the Cu+CNT particles was 14 m^2/g compared to the 7.9 m^2/g of the TEM surface area. The TEM surface area is calculated from the particles in the sample, only omitting the CNT-like structures. This is clearly the reason for the higher BET surface area compared to the TEM size distribution calculation. The comparable Cu+C surface area with the same 0.92 mol-% ethene concentration is 7.8 m^2/g.

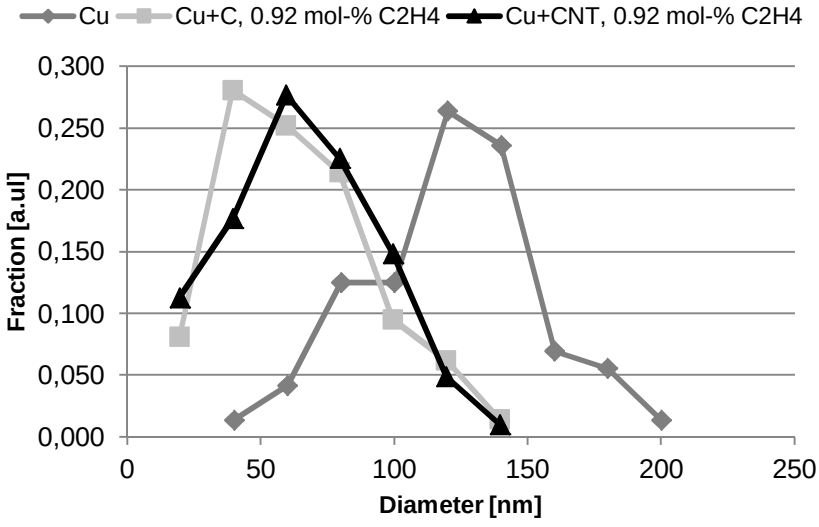

Figure 3.17. Size distributions of Cu, Cu+C, and Cu+CNT particles. The ethene concentration was 0.92 mol-% for Cu+C and Cu+CNT particles.

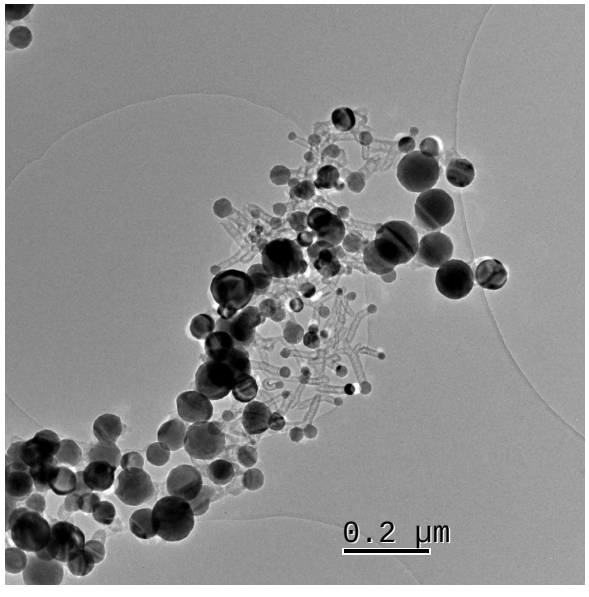

Figure 3.18. TEM micrograph showing copper particles and CNT-like structures. The ethene concentration was 0.92 mol-% and the water concentration 1.2 mol-%.

3.5 Magnetic properties of Co and Co+C particles

The saturation magnetisation of the Co and Co+C particles is very similar to that of bulk Co ($M_{s,\ bulk}$ = 159 emu/g (Economou 2010). This is seen in Table 3-5 (Publication III). The coercive field and remnant magnetisation of all Co and Co+C particles are negligibly small, indicating the formation of a multidomain state with zero net magnetisation in the absence of an external magnetic field. In the particles larger than the single-domain size, multidomains form, and if magnetic domain wall motion is efficient, this can completely eliminate hysteretic magnetic switching. In our experiments, the particle sizes are clearly in the multidomain regime for all but the 17 nm sample, and thus the observations of zero coercive field and remanent magnetisation indicate efficient magnetic domain wall motion. An example of the measured hysteresis curves is shown in Figure 3.19, which depicts magnetisation reversal in Co+C nanoparticles with NAD 40 nm. The carbon shell on the particles may also act as a lubricant and thus the particles could freely rotate during the magnetic measurement. This would significantly reduce the observed hysteresis. For bulk Co, the coercive field is 1 mT (Brown 1958).

Table 3-5. The saturation moment density and coercive field for Co, Co+C and particles.

Material	NAD (nm)	M_S (emu/g)	H_R (mT)	Remanence (%)
Co	76	149	0	0
Co	46	146	0	0
Co	33	147	0	0
Co+C	40	141	0	0

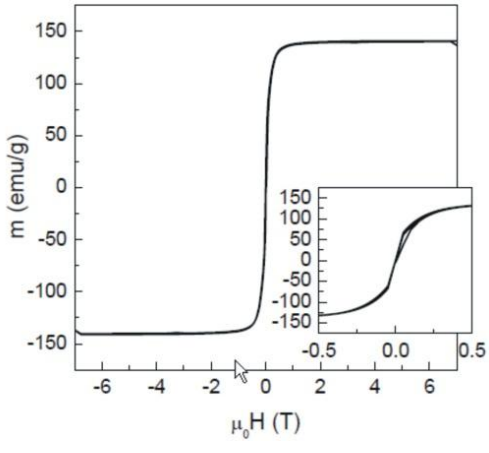

Figure 3.19. The magnetic hysteresis loop for Co+C particles with NAD 40 nm. (Publication III)

The steepest slope in Figure 3.19 is 800 emu/gT. When this is converted to SI units and inserted into Equations 2 and 4, the relative permeability can be estimated with $\mu_R = 10$. A typical value for bulk Co is about 100 (Brown 1958). The lower permeability is a result of the measurement of an unpressed powder sample. The density of the sample is a few per cent of the density of the bulk Co, due to a large amount of air in the sample. In a large multidomain structure, the force of the neighbouring domains first opposes but then strengthens the change of magnetic orientation as the direction of the external field is switched. The number of domains within a nanoparticle is small and the coupling between particles much weaker than the coupling between domains in the same crystal. Especially weak is the interaction when the distance between particles increases, as in an unpressed powder.

4. Applications

4.1 Preparation and characterisation of applications

The conductive ink was prepared at VTT (Kim Eiroma, Eva-Lena Hult Mori). The antenna substrates were prepared at the University of Oulu (Merja Teirikangas, Ari Juuti). The preparation processes and results are explained briefly below, since proper analysis of particle properties requires inclusion of ink and substrate properties.

4.1.1 Conductive ink

The conductive ink was prepared by dispersing the Cu+C and Cu+CNT particles with dispersants in a mixed solvent (Publication IV). The dispersants were three high molecular weight dispersing agents, DISPERBYK-190, DISPERBYK-198, and DISPERBYK-2012, intended for water-based carbon black pigment dispersions by BYK Chemie Gmbh. De-ionised water (DIW) was used as the main solvent. Ethylene glycol monomethyl ether (EGME) (Sigma-Aldrich), ethylene glycol monobuthyl ether (EGBE) (Merck), and n-propanol (Honeywell Riedel-de Haen) were used as co-solvents.

The mixed suspension was sonicated for 10 minutes in an ice bath using a UP400S ultrasonic processor (Hielscher Ultrasonics). Thereafter, the suspension was left to settle for an hour, followed by decanting. Prior to spin coating or printing, the suspension was sonicated in an ultrasonic bath for 10 minutes.

Spin coating of the nanoparticle dispersions was carried out using an EC101D series spin coater (Headway Research) at 1000 rpm for 1 minute. Inkjet printing was carried out with a DMP-2831 laboratory-scale piezoelectric drop-on-demand printer (Fujifilm Dimatix). Layers were deposited on microscopic glass slides (Thermo Scientific**)**. A single layer for both inkjet printing and spin coating was applied. The spin-coated and printed layers were immediately dried on a hot plate for 60–90 seconds at 60°C. Then they were dried in an oven at 105°C in air for 1 hour. For electrical conductance characterisation, gold electrode pairs were grown by thermal vacuum evaporation on the deposited copper-carbon layers.

The topographies of the dried spin-coated and printed layers were characterised by SEM imaging (LEO DSM 982 FE-SEM and LEO Supra 35 FE-SEM). Electrical characterisation of the dried copper-carbon layers was performed by 2-point

probe resistance measurements from the thermal vacuum evaporated gold electrodes using a digital multimeter (Agilent 34411A). The temperature-resistance dependence was measured using a setup consisting of a closed chamber precision-controlled temperature ramping hot plate (Instec HCP622V) and a data acquisition/switch unit (Agilent 34970A) for on-line 2-point probing.

4.1.2 Antenna substrates

For antenna substrates (Publication II), the target was to prepare composites where metal particles are well dispersed and not connected to each other. The composites were compounded using a twin-screw mixing extruder (Haake Minilab, Thermo Electron Co.). The matrix was a thermoplastic polymer ER182 (ρ = 0.92 g/cm^3, NOF Co., Japan). Filler materials were Co and Co+C particles. The compounding temperature was 220°C and the compounding time 15 minutes. The final filler content of the fabricated composites (Co-ER182 and Co-C-ER183) was measured by the Archimedes method with a pycnometer (Gay-Lssac Blaubrand®, BRAND GmbH + Co KG). Permeabilities of the composites were measured using an Agilent E4991A RF Impedance/Material analyser from 1 MHz to 1 GHz. The homogeneity of the nanoparticle distributions in the polymer matrix was studied with a field emission scanning electron microscope (FESEM, Zeiss ULTRA plus, Carl Zeiss SMT AG, Germany).

4.2 Properties of applications

4.2.1 Conductive ink

Several ink formulations were tested with Cu+C nanoparticles. The optimised fluid was found to be a 25–25–25 wt.-% water/EGBE/n-propanol mixture with 25 wt.-% Cu+CNT nanoparticles, and stabilised by a polymeric dispersing agent (DISPERBYK-198, 8 wt.-% of particle mass). A conductivity of 6.4 S/m was obtained with a single deposited layer without sintering or high-temperature annealing. A higher amount of dispersing agent decreased conductivity rapidly. This is likely due to complete coverage of the particles by the dispersing agent, so that no particle-particle contacts are formed in the dried layer. The conductivity of the sample remained unchanged throughout the heating cycles from 25–100°C (Figure 4.1). The dried ink layer is shown in Figure 4.2. The particles are separate and well dispersed. The line width of the inkjet-printed lines was 150 µm. The inks made of Cu+CNT particles were more stable than those made of Cu+C particles. The nanotube-like structures improved dispersion.

The copper particles did not oxidise in the water-based solutions or during the drying of the ink. This further strengthens the conclusion that the particles are uniformly covered with a protective carbon layer. The CNT-like structures may create bridges between particles through the dispersants and thus increase the

conductivity of the ink. The CNT-like structures may also act as dispersants, increasing the effective volume of the particle.

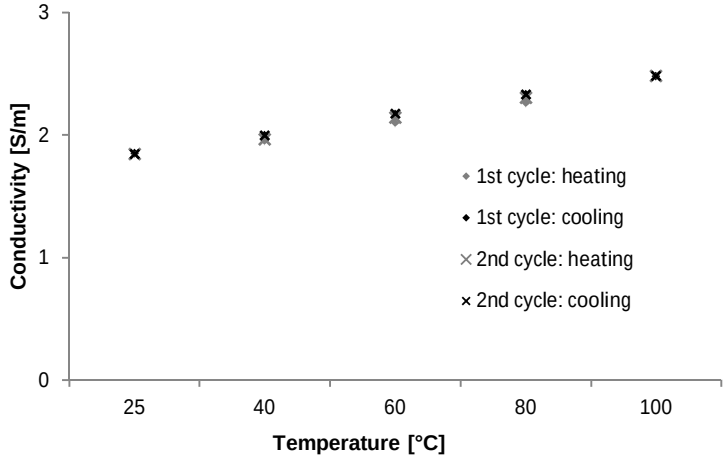

Figure 4.1. Conductivity of dried spin-coated ink as a function of temperature. The conductivity remained unchanged for two heating cycles up to 100°C. (Publication IV)

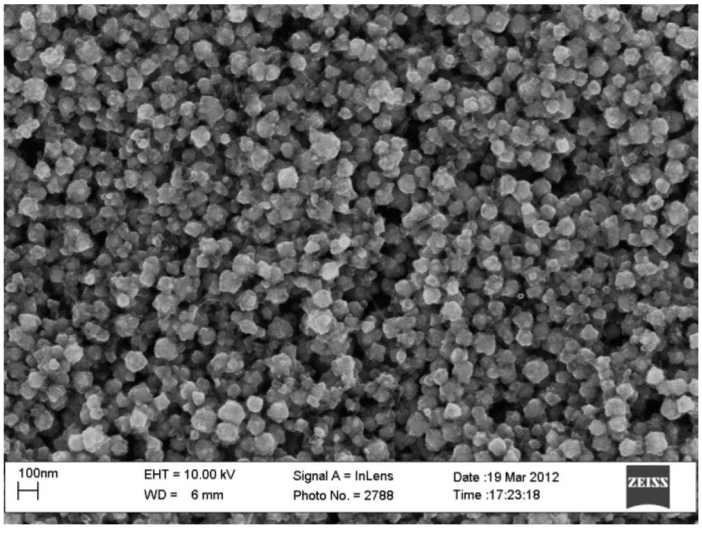

Figure 4.2. SEM image of dried spin-coated ink made of Cu+CNT nanoparticles.

4.2.2 Antenna substrates

The permeability of the nanoparticle-polymer complex increased as expected. As the fraction of particles in the complex was increased, the permeability and loss tangent of the complex increased. When studied as a function of frequency, the relative permeability and magnetic losses increased slightly towards higher frequencies in both Co-ER182 and Co-C-ER182. The rate of increase is faster with carbon-coated particles when filler loading was further increased. The observed behaviour can be attributed partly to the smaller size of the coated particles: it is known that eddy currents induced by a high-frequency electromagnetic field decrease with decreasing particle size (Ramprasad et al. 2004).

For the Co particles, the measured permeability values of Table 4-1 are compared to the reluctance and Bruggeman theories in Figure 4.3. The reluctance theory is found to be in reasonable agreement with the measured behaviour for these samples. However, the data does not allow definitive conclusions. The observed permeabilities and magnetic losses are similar to those observed by Wu et al. (2002) and Brosseau and Talbot (2005). Wu et al. used SiO_2-coated 40 nm Co particles dispersed in wax, whereas Brosseau and Talbot used 21 nm Co in epoxy.

The FESEM analysis showed that although a majority of the particles in the matrix were separated and homogeneously dispersed, some particle chains and agglomerates could be observed. The formed particle chains typically consisted of 5–10 particles and were orientated in the direction of the injection flow.

The relative permeability of the particles in the calculations for Figure 4.3 was 100, a typical Co bulk value. However, for these particles, 10 is a better estimate, as calculated in Chapter 3.5. Using 10 would lead to lower permeability of the composite and thus a discrepancy from the experimental results. However, in the calculations, the density of the particles is set to the bulk density of the metal. The volume fractions shown in Table 4-1 and Figure 4.3 are based on the metal nanoparticle powder, which has a much lower density. The air in the metal nanoparticle powder escapes the polymer and is not included in the final product.

Table 4-1. Relative permeability and magnetic losses for metal nanoparticle-polymer composites

Filler particles	Filler loading vol-%	μr	tan δμ
	0	1.04	0.0002
Co	3	1.35	0.0554
Co	8	1.65	0.0556
Co	15	1.96	0.076
Co	20	2.29	0.098
Co	29	3.07	0.1527
Co+C	8	1.8	0.042
Co+C	13	2.54	0.1237
Co+C	15	3.78	0.2

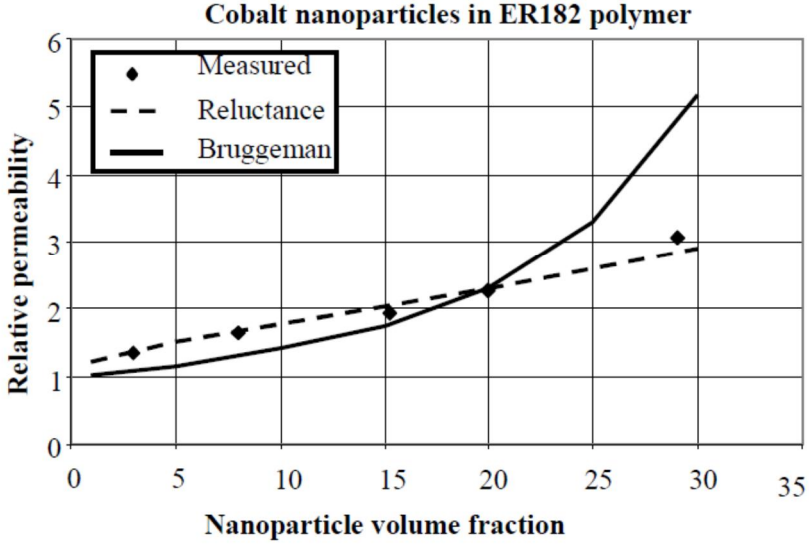

Figure 4.3. Relative permeability of the Co nanoparticle-polymer composite as a function of the nanoparticle volume fraction. The experimental data is compared to the Bruggeman and Reluctance theories (Publication II).

5. Conclusions

Metal nanoparticles have thrilling properties that are not found in bulk scale materials. As the ratio of surface atoms to bulk atoms increases, reactivity increases, magnetic properties are changed and new processing techniques may be employed. These properties enable new applications such as those presented in this thesis.

Hydrogen reduction of metal chlorides is a very effective technique for producing Co, Ni, and Cu nanoparticles. The simple modelling left a few options for the formation mechanisms of the particles. If the surface reaction has no significant role in the growth of the particles, then the gas-phase reaction rate is much faster than previously reported. If both the gas-phase and surface reaction contribute to final conversion, the gas-phase reaction rate may be equal to earlier experiments, but not slower. If the surface-reaction rate governs total conversion, the gas-phase reaction can be much slower than previously reported and backward reaction almost as fast as forward reaction. In all cases, only a minimum of the gas-phase reaction rate can be obtained with the simple method used. However, concluding from all the experimental results, the most likely scenario is that both the gas-phase and surface reaction contribute to the conversion of metal chloride to metal.

The Co and Cu nanoparticles can be coated with carbon if ethene is added to the reaction flow. Ethene decomposes catalytically on the nanoparticle surface and creates a shell on the particles Therefore, changing the ratio of the metal chloride and ethene changes the balance of the competing surface reactions of metal chloride reduction and ethene decomposition. In this way, the number average diameter of the primary particles can also be controlled while mass concentration is kept constant.

The saturation magnetisation of the Co and Co+C particles is almost equal to bulk Co. The measured coercive field and remanent magnetisation was zero. These result from particle size and are due to the fact that the particles were not bound to any matrix. The Co and Co+C particles can be applied in antenna substrates. The relative permeability of the nanoparticle-polymer composite follows reluctance theory, even though some particle chains were observed in the samples. The theory is only valid for uniformly dispersed non-agglomerated particles.

In the case of copper particles, the growth of CNT-like structures can be promoted with the addition of water to the reaction flow. Water cleans the particle

surface of graphitic carbon and increases the reaction rate of copper chloride to metallic copper.

It has been demonstrated that the Cu+C and Cu+CNT particles can be used to produce a conductive ink for antistatic use. It is vital for this conductivity that the particle-particle distance is minimised. On the other hand, the dispersants should not cover the particles so well that a thick resistant layer would be formed on top of the particles. The balance between good dispersion and a short particle-particle distance is delicate.

Hydrogen reduction has been proven to be an effective method of producing Co, Ni, and Cu particles for various applications. The carbon coating enables the formulation of inks and protects the particles against oxidation. In future, the carbon-coated Co, Ni, and Cu particles can be used in many other applications through bonding to the carbon coating in the same way that was used for ink fabrication or through polymer composites.

The scaling of the particle production for applications has a higher likelihood of success if the formation mechanics of the particles are precisely known. The correct mechanism should be found out with a comprehensive set of experiments. The backward reaction rate in this experimental setup could be found by feeding cobalt particles and HCl into the reactor without hydrogen and $CoCl_2$. In addition, an experiment where additional HCl (various proportions) was fed into the reactor in addition to $CoCl_2$ and H_2 should be conducted. The importance of surface reaction could be verified by feeding initial cobalt particles together with cobalt chloride and hydrogen into the reactor. Experiments with a decreased reaction time and thus less complete reactions would also be needed. These experiments should be completed separately for Ni and Cu to find out the parameters of $NiCl_2$ and CuCl reduction.

References

AALTONEN, T., RITALA, M., SAMMELSELG, V. and LESKELÄ, M., 2004. Atomic Layer Deposition of Iridium Thin Films. Journal of the Electrochemical Society, 151(8), pp. G489–G492.

ANSI ESD S541-2008. For the Protection of Electrostatic Discharge Susceptible Items: Packaging Materials for ESD Sensitive Items. Washington, D.C. www.ansi.org.

ATHANASSIOU, E.K., GRASS, R.N. and STARK, W.J., 2006. Large-scale production of carbon-coated copper nanoparticles for sensor applications. Nanotechnology, 17(6), pp. 1668.

BONARD, J., SERAPHIN, S., WEGROWE, J., JIAO, J. and CHÂTELAIN, A., 2001. Varying the size and magnetic properties of carbon-encapsulated cobalt particles. Chemical Physics Letters, 343(3–4), pp. 251–257.

BREWER, L. and LOFGREN, N., 1950. The Thermodynamics of Gaseous Cuprous Chloride, Monomer and Trimer. Journal of American Chemical Society, 72(7), pp. 3038–3045.

BRILLO, J. and EGRY, I., 2005. Surface tension of nickel, copper, iron and their binary alloys. Journal of Materials Science, 40(9–10), pp. 2213–2216.

BROSSEAU, C. and TALBOT, P., 2005. Effective magnetic permeability of Ni and Co micro- and nanoparticles embedded in a ZnO matrix. Journal of Applied Physics, 97(10), p. 104325.

BROWN, W.F., 1958. Ch 8 Magnetic Materials. In: E. CONDON and H. ODISHAW (Eds.), Handbook of Chemistry and Physics. McGraw-Hill.

BÜSSER, B.A., 2011. Multiscale Design for Aerosol Synthesis of Functional Nanoparticles, ETH Zürich.

CHAMBERS, A. and BAKER, R.T., 1997. Influence of Chlorine on the Decomposition of Ethylene over Iron and Cobalt Particles. The Journal of Physical Chemistry B, 101(9), pp. 1621–1630.

CHEN, J.P., SORENSEN, C.M. and KLABUNDE, K.J., 1995. Enhanced magnetization of nanoscale colloidal cobalt particles. Physical Review B, 51, p. 11527.

CHEN, Y., PENG, D., LIN, D. and LUO, X., 2007. Preparation and magnetic properties of nickel nanoparticles via the thermal decomposition of nickel organometallic precursor in alkylamines. Nanotechnology, 18(50), pp. 505703.

CHIANG, C., AROH, K., FRANSON, N., SATSANGI, V.R., DASS, S. and EHRMAN, S., 2011. Copper oxide nanoparticle made by flame spray pyrolysis for photoelectrochemical water splitting – Part II. Photoelectrochemical study. International Journal of Hydrogen Energy, 36(24), pp. 15519–15526.

DUGLEUX, P. and DE ALMEIDA MARQUES, S., 1980. Preparation of metal powders of groups VI and VIII (Fe, Co, Ni) by the vapor phase reduction of their chlorides pure or in binary mixtures. Powder Technology, 27(1), pp. 45–52.

ECONOMOU, E.N. 2010. Magnetic Materials, I: Phenomenology. Springer Berlin Heidelberg.

EGGEMAN, A.S., PETFORD-LONG, A.K., DOBSON, P.J., WIGGINS, J., BROMWICH, T., DUNIN-BORKOWSKI, R. and KASAMA, T., 2006. Synthesis and characterisation of silica encapsulated cobalt nanoparticles and nanoparticle chains. Journal of Magnetism and Magnetic Materials, 301(2), pp. 336–342.

FRIEDLANDER, S.K., 2000. Smoke, dust, and haze: fundamentals of aerosol dynamics. New York: Oxford University Press.

FU, W., YANG, H., HARI-BALA, LIU, S., LI, M. and ZOU, G., 2006. Preparation and characteristics of core–shell structure cobalt/silica nanoparticles. Materials Chemistry and Physics, 100(2–3), pp. 246–250.

GALLOIS, B. and LUPIS, C.H.P., 1981. Effect of oxygen on the surface tension of liquid copper. Metallurgical Transactions B, 12(3), pp. 549–557.

GELATOS, A.V., MARSH, R., KOTTKE, M. and MOGAB, C.J., 1993. Chemical vapor deposition of copper from Cu[sup + 1] precursors in the presence of water vapor. Applied Physics Letters, 63(20), pp. 2842–2844.

GILLEO, K., 1996. Polymer Thick Film. New York: Van Nostrand Reinhold.

GOO, Y., LEE, Y., KIM, N., LEE, K., YOO, B., HONG, S., KIM, J. and CHOA, Y., 2010. Ink-jet printing of Cu conductive ink on flexible substrate modified by oxygen plasma treatment. Surface and Coatings Technology, 205, Supplement 1, pp. S369–S372.

GOUBERT-RENAUDIN, S.N.S. and WIECKOWSKI, A., 2011. Ni and/or Co nanoparticles as catalysts for oxygen reduction reaction (ORR) at room temperature. Journal of Electroanalytical Chemistry, 652(1–2), pp. 44–51.

GUBIN, S.P., 2009. Magnetic Nanoparticles. John Wiley & Sons.

HSIEN-HSUEH, L., KAN-SEN, C. and KUO, 2005. Inkjet printing of nanosized silver colloids. Nanotechnology, 16(10), p. 2436.

JANG, H.D., HWANG, D.W., KIM, D.P., KIM, H.C., LEE, B.Y. and JEONG, I.B., 2003. Preparation of Cobalt Nanoparticles in the Gas Phase (I): Kinetics of Cobalt Dichloride Reduction. Journal of Industrial Engineering Chemistry, 9(4), p. 407.

JANG, H.D., HWANG, D.W., KIM, D.P., KIM, H.C., LEE, B.Y. and JEONG, I.B., 2004. Preparation of cobalt nanoparticles by hydrogen reduction of cobalt chloride in the gas phase. Materials Research Bulletin, 39(1), pp. 63–70.

JENSEN, J.H., MOROKUMA, K. and GORDON, M.S., 1994. Pathways for H2 elimination from ethylene: a theoretical study. Journal of Chemical Physics, 100(3), p. 1981.

JEONG, S., WOO, K., KIM, D., LIM, S., KIM, J.S., SHIN, H., XIA, Y. and MOON, J., 2008. Controlling the Thickness of the Surface Oxide Layer on Cu Nanoparticles for the Fabrication of Conductive Structures by Ink-Jet Printing. Advanced Functional Materials, 18(5), pp. 679–686.

JUN, Y., SEO, J. and CHEON, J., 2008. Nanoscaling Laws of Magnetic Nanoparticles and Their Applicabilities in Biomedical Sciences. Accounts of Chemical Research, 41(2), pp. 179–189.

JUN, S., UHM, Y.R., RHEE, C.K., SONG, R., PARK, S. and KIM, H., 2011. Preparation of Carbon-encapsulated Ag Nanoparticles for Dispersion in La0.5Sr0.4Co0.3Fe0.7O3-d. Journal of the Koreal Physical Society, 59(6), pp. 3648–3651.

KARÂKINA, L.E., KARÂKIN, I.N. and GORNOSTYREV, Y.N., 2010. Process of faceting in nanoparticles of FCC metals: Results of simulation by the molecular-dynamics method. The Physics of Metals and Metallography, 109(3), pp. 211–219.

KATO, Y., SUGIMOTO, S., SHINOHARA, K., TEZUKA, N., KAGOTANI, T. and KOICHIRO, I., 2002. Magnetic properties and microway absoprtion properties of polymer-coated cobalt particles. Materials Transactions, 43(3), pp. 406–409.

KEKESI, T., MIMURA, K. and ISSHIKI, M., 1995. Copper Extraction from Chloride Solutions by Evaporation and Reduction with Hydrogen. Materials Transaction, 36(5), pp. 649–658.

LUECHINGER, N.A., ATHANASSIOU, E.K. and STARK, W.J., 2008. Graphene-stabilized copper nanoparticles as an air-stable substitute for silver and gold in low-cost ink-jet printable electronics. Nanotechnology, 19(44), pp. 445201.

MAGDASSI, S., GROUCHKO, M. and KAMYSHNY, A., 2010. Copper nanoparticles for Printed Electronics: Routes Towards Achieving Oxidation Stability. Materials, 3(9), pp. 4626–4638.

MALE, K.B., HRAPOVIC, S., LIU, Y., WANG, D. and LUONG, J.H.T., 2004. Electrochemical detection of carbohydrates using copper nanoparticles and carbon nanotubes. Analytica Chimica Acta, 516(1–2), pp. 35–41.

MILLER, K.J., COLLIER, K.N., SOLL-MORRIS, H.B., SWAMINATHAN, R. and MCHENRY, M.E., 2009. Induction heating of FeCo nanoparticles for rapid rf curing of epoxy composites. Journal of Applied Physics, 105(7), pp. 07E714-07E714-3.

MÜLLER, J., SÖNNICHSEN, C., VON POSCHINGER, H., VON PLESSEN, G., KLAR, T.A. and FELDMANN, J., 2002. Electrically controlled light scattering with single metal nanoparticles. Applied Physics Letters, 81(1), p. 171.

NARKIEWICZ, U. and PODSIADŁY, M., 2010. Synthesis of carbon-encapsulated nickel nanoparticles. Applied Surface Science, 256(17), pp. 5249–5253.

NARKIEWICZ, U., PODSIADŁY, M., JĘDRZEJEWSKI, R. and PEŁECH, I., 2010. Catalytic decomposition of hydrocarbons on cobalt, nickel and iron catalysts to obtain carbon nanomaterials. Applied Catalysis A: General, 384(1–2), pp. 27–35.

NASIBULIN, A.G., MOISALA, A., BROWN, D.P. and KAUPPINEN, E.I., 2003. Carbon nanotubes and onions from carbon monoxide using Ni(acac)2 and Cu(acac)2 as catalyst precursors. Carbon, 41(14), pp. 2711–2724.

NASIBULIN, A.G., BROWN, D.P., QUEIPO, P., GONZALEZ, D., JIANG, H. and KAUPPINEN, E.I., 2006. An essential role of CO2 and H2O during single-walled CNT synthesis from carbon monoxide. Chemical Physics Letters, 417(1–3), pp. 179–184.

PALASANTZAS, G., VYSTAVEL, T., KOCH, S.A. and DE HOSSON, J. TH. M., 2006. Coalescence aspects of cobalt nanoparticles during in situ high-temperature annealing. Journal of Applied Physics, 99(2), p. 024307.

PARK, B.K., KIM, D., JEONG, S., MOON, J. and KIM, J.S., 2007. Direct writing of copper conductive patterns by ink-jet printing. Thin Solid Films, 515(19), pp. 7706–7711.

PYYKÖNEN, J., 2001. Computational simulation of aerosol behaviour, Helsinki University of Technology.

RAJ, P.M., SHARMA, H., REDDY, G.P., REID, D., ALTUNYURT, N., SWAMINATHAN, M., TUMMALA, R. and NAIR, V., 2011. Novel nanomagnetic materials for high-frequency RF applications, IEEE 61st Electronic Components and Technology Conference (ECTC), May 31st – Jun 3rd 2011, pp. 1244–1249.

RAMPRASAD, R., ZURCHER, P., PETRAS, M., MILLER, M. and RENAUD, P., 2004. Magnetic properties of metallic ferromagnetic nanoparticle composites. Journal of Applied Physics, 96(1), pp. 519–529.

RODRIGUES, E.L. and BUENO, J.M.C., 2002. Co/SiO2 catalysts for selective hydrogenation of crotonaldehyde II: influence of the Co surface structure on selectivity. Applied Catalysis A: General, 232(1–2), pp. 147–158.

ROVEIMIAB, Z., MAHDAVIAN, A.R., BIAZAR, E. and HEIDARI, K.S., 2012. Preparation of Magnetic Chitosan Nanocomposite Particles and Their Susceptibility for Cellular Separation Applications. J. Colloid. Sci. Biotechnol., 1, p. 82.

SCHAPER, A.K., HOU, H., GREINER, A., SCHNEIDER, R. and PHILLIPP, F., 2004. Copper nanoparticles encapsulated in multi-shell carbon cages. Applied Physics A: Materials Science & Processing, 78(1), pp. 73–77.

SERBAN, M., LEWIS, M. and BASCO, J., 2004. Kinetic Study of Hydrogen and Oxygen Production Reactions in the Copper Chloride Thermochemical Cycle, AIChE 2004 Spring National Meeting, April 25th – 29th 2004.

SHAO, H., HUANG, Y., LEE, H., SUH, Y.J. and KIM, C.O., 2006. Cobalt nanoparticles synthesis from Co(CH3COO)2 by thermal decomposition. Journal of Magnetism and Magnetic Materials, 304(1), pp. e28–e30.

SUBRAMANIAN, N.D., BALAJI, G., KUMAR, C.S.S.R. and SPIVEY, J.J., 2009. Development of cobalt–copper nanoparticles as catalysts for higher alcohol synthesis from syngas. Catalysis Today, 147(2), pp. 100–106.

SUH, Y.J., JANG, H.D., CHANG, H.K., HWANG, D.W. and KIM, H.C., 2005. Kinetics of gas phase reduction of nickel chloride in preparation for nickel nanoparticles. Materials Research Bulletin, 40(12), pp. 2100–2109.

TANABE, K., 2007. Optical radiation efficiencies of metal nanoparticles for optoelectronic applications. Materials Letters, 61(23–24), pp. 4573–4575.

TOMITA, S., HIKITA, M., FUJII, M., HAYASHI, S. and YAMAMOTO, K., 2000. A new and simple method for thin graphitic coating of magnetic-metal nanoparticles. Chemical Physics Letters, 316(5–6), pp. 361–364.

TÖRNDAHL, T., OTTOSSON, M. and CARLSSON, J., 2004. Growth of copper metal by atomic layer deposition using copper(I) chloride, water and hydrogen as precursors. Thin Solid Films, 458(1–2), pp. 129–136.

WANG, S., XIE, F. and HU, R., 2007. Carbon-coated nickel magnetic nanoparticles modified electrodes as a sensor for determination of acetaminophen. Sensors and Actuators B: Chemical, 123(1), pp. 495–500.

WANG, Z.H., CHOI, C.J., KIM, B.K., KIM, J.C. and ZHANG, Z.D., 2003. Characterization and magnetic properties of carbon-coated cobalt nanocapsules synthesized by the chemical vapor-condensation process. Carbon, 41(9), pp. 1751–1758.

WILLIAMS, B.W., Soft magnetic materials. Power Electronics. University of Strathclyde, p. 617.

VOLLATH, D., 2007. Plasma Synthesis of Nanoparticles. Kona, 25, pp. 39–55.

WU, M., ZHANG, Y.D., HUI, S., XIAO, T.D., GE, S., HINES, W.A., BUDNICK, J.I. and TAYLOR, G.W., 2002. Microwave magnetic properties of Co50/(SiO2)50 nanoparticles. Applied Physics Letters, 80(23), pp. 4404–4406.

WU, H., CAO, W., LI, Y., LIU, G., WEN, Y., YANG, H. and YANG, S., 2010. In situ growth of copper nanoparticles on multiwalled carbon nanotubes and their application as non-enzymatic glucose sensor materials. Electrochimica Acta, 55(11), pp. 3734–3740.

XU, Q., ZHAO, Y., XU, J.Z. and ZHU, J., 2006. Preparation of functionalized copper nanoparticles and fabrication of a glucose sensor. Sensors and Actuators B: Chemical, 114(1), pp. 379–386.

XU, Y., MAHMOOD, M., LI, Z., DERVISHI, E., TRIGWELL, S., ZHAROV, V.P., ALI, N., SAINI, V., BIRIS, A.R., LUPU, D., BOLDOR, D. and BIRIS, A.S., 2008. Cobalt nanoparticles coated with graphitic shells as localized radio frequency absorbers for cancer therapy. Nanotechnology, 19(43), p. 435102.

YAO, W.J., HAN, X.J., CHEN, M., WEI, B. and GUO, Z.Y., 2002. Surface tension of undercooled liquid cobalt. Journal of Physics: Condensed Matter, 14(32), p. 7479.

ZENGYUN, J., KAZUHIKO, K. and WANQI, J., 2002. Solid-liquid Interface Energy of Metals at Melting Point and Undercooled State. Materials Transactions, 43(4), pp. 721–726.

ZHAI, J., TAO, X., PU, Y., ZENG, X. and CHEN, J., 2011. Controllable synthesis and characterization of novel copper–carbon core–shell structured nanoparticles. Materials Research Bulletin, 46(6), pp. 865–870.

ZHOU, W., HAN, Z., WANG, J., ZHANG, Y., JIN, Z., SUN, X., ZHANG, Y., YAN, C. and LI, Y., 2006. Copper Catalyzing Growth of Single-Walled Carbon Nanotubes on Substrates. Nano Letters, 6(12), pp. 2987–2990.

Appendix A: Condensation heat flux

In this appendix, an order of magnitude calculation is shown of the condensation heat flux to the particles and the radiation heat transfer away from the particles. The purpose is to show that the condensation heat flux does not increase the temperature of the particles to a level that would enable sintering of the formed particles.

One simple calculation is performed. The particle concentration c_n is assumed to be $3.8 \cdot 10^{15}$ 1/m^3, as in the model. The particle diameter is set to 30 nm, as at this point in the reaction the particle cores have formed and if the reaction was mainly a gas-phase reaction, they would grow by condensation at a fast rate. The mass of one particle is $m_{particle} = \rho V_{particle} = \rho \cdot 4/3\pi \cdot (d/2)^3 = 1.27^{-16}$ g. The heat of vaporisation is H_v = 370 kJ/mol or $6.14 \cdot 10^{-22}$ J/atom for Co. The formation rate of Co atoms, when the particle diameter is 30 nm in the model, is $f_{Co} = 1 \cdot 10^{23}$ 1/m^{3}s for k_1 = 300 1/min and k_3 = 0. Assuming that the condensation rate is equal to the formation rate (very low saturation vapour pressure of Co), this leads to condensation flow for one particle of $Q_{\text{particle}} = f_{Co}/c_n = 2.6 \cdot 10^7$ Co atoms/s. Then the condensation heat flux for one particle is $P_{condensation} = Q_{particle} \cdot H_{v,a} = 1.6 \cdot 10^{-11}$ J/s. It is important to note that even though the figures are given as 1/s, the relevant time scale is 0.1s.

The radiation heat flux $P_{radiation}$ is given by:

$$P_{radiation} = \epsilon \sigma_{SB} A_{particle} T^4 \tag{19}$$

Here, $\sigma_{SB}=5.67 \cdot 10^{-8}$ W/m^{2}K^4. For a 30 nm particle diameter and a 950°C temperature, this gives $3.6 \cdot 10^{-10}$ J/s, and for a 1000°C temperature $4.2 \cdot 10^{-10}$ J/s. Here, ε is assumed to be 1. The difference is $6.2 \cdot 10^{-11}$ J/s. The actual value for ε can be smaller, but the result is in the same order of magnitude as the condensation heat flux. This means that an increase of only 50 degrees in particle temperature relative to reaction temperature is enough to compensate for the condensation heat flux by radiation heat flux. Therefore, the temperature of the particles is not much higher than the reaction temperature, independently of whether the particles grow by condensation or surface reaction.

Series title and number
VTT Science 36

Title	**Production of Co, Ni, and Cu nanoparticles by hydrogen reduction**
Author(s)	Johanna Forsman
Abstract	In this thesis, production of Co, Ni, and Cu nanoparticles by hydrogen reduction of metal chlorides in gas phase was studied. Nanoparticles have unique properties not found in bulk or micron-scale materials. These enable new products or reduced use of raw materials. Metal nanoparticle production has been studied widely, but especially for coated metal particles, research of coating mechanisms and economic production methods is still needed. The method used in this thesis combines a high yield, a high production rate, low production costs, high particle quality, and a good range of available particle number average diameters and other properties. These particles could be utilised in conductive inks, antenna substrates, medical imaging, or as sensors and catalysts. The number average primary particle diameter (NAD) of Co particles increased from 20 to 84 nm as the particle mass concentration increased from 0.5 to 10 g/m^3. For even higher particle mass concentrations, the NAD did not increase. The Co and Cu particles were coated in-situ with carbon, by adding ethene to the reaction flow. Copper particles were also coated with carbon and carbon nanotube-like structures by adding ethene and water to the reaction flow. When ethene concentration was increased from zero to 9.2 mol-%, the NAD decreased from 84 to 17 nm for cobalt. Particle mass concentration was 10 g/m^3 or higher in these experiments. The standard deviation was 17 nm when NAD 84 nm and 7 nm when NAD was 17 nm. For copper, the NAD increased from 20 to121 nm. The particles were crystalline with an FCC structure in all cases. The particle growth was modelled in a simplified way. It appears, that surface reaction is an important part of the particle growth process. The most likely scenario is that first, seed particles form by gas phase reaction and nucleation. Then, these particles grow partly by surface reaction and partly by condensation growth. In the gas phase, some backward reaction of metal to metal chloride occurs. The saturation magnetic moment of the Co and Co+C particles was 141–147 emu/g, which is close to bulk Co (159 emu/g). No hysteresis was observed for these particles. Cobalt particles with and without carbon coating were used to fabricate polymer composites, which could be applied in RF antennae. The relative permeability of the composite was increased from 1 to 3 as the loading of the particles increased from zero to 28 vol-%. Copper particles coated with carbon coating and CNT-like structures were used to fabricate inkjet fluid capable of producing conductive lines after printing a single layer. The best achieved conductivity was 6.4 S/m.
ISBN, ISSN	ISBN 978-951-38-8007-1 (Soft back ed.) ISBN 978-951-38-8008-8 (URL: http://www.vtt.fi/publications/index.jsp) ISSN-L 2242-119X ISSN 2242-119X (Print) ISSN 2242-1203 (Online)
Date	August 2013
Language	English, Finnish abstract
Pages	62 p. + app. 51 p.
Keywords	Cobalt, copper, nickel, nanoparticles, core-shell, magnetic nanoparticles
Publisher	VTT Technical Research Centre of Finland P.O. Box 1000, FI-02044 VTT, Finland, Tel. 020 722 111

Julkaisun sarja ja numero
VTT Science 36

Nimeke	**Co-, Ni- ja Cu-nanohiukkasten tuotto vetypelkistysmenetelmällä**
Tekijä(t)	Johanna Forsman
Tiivistelmä	Tässä väitöskirjatyössä on tutkittu kobolttі-, nikkeli- ja kuparinanohiukkasten tuottoa vetypelkistysmenetelmällä kaasufaasissa. Nanomateriaaleilla on ominaisuuksia, joita ei ole vastaavilla isomman kokoluokan materiaaleilla. Niiden avulla voidaan tehdä uudenlaisia tuotteita tai vähentää materiaalien käyttöä ratkaisevasti. Lähtöaineena on käytetty metalliklorideita. Metallinanohiukkasten tuottoa on tutkittu paljon, mutta erityisesti päällystettyjen hiukkasten tapauksessa tarkkoja ja taloudellisia menetelmiä on edelleen syytä tutkia ja kehittää. Tässä työssä käytetyllä menetelmällä voidaan tuottaa hiukkasia niin, että hiukkaskoon ja muita muuttujia voi valita samalla, kun hiukkasten laatu ja tuotto pysyvät korkealla. Kobolttihiukkasten lukumääräkeskiarvostettu primäärihiukkashalkaisija (LKH) kasvoi 20 nanometristä 84 nanometriin, kun hiukkasten massakonsentraatio kasvoi arvosta 0,5 g/m3 arvoon 10 g/m3. Tätä suuremmilla massakonsentraatioilla hiukkaset eivät enää kasvaneet. Koboltti- ja kuparihiukkaset päällystettiin hiilellä lisäämällä eteeniä reaktiovirtaukseen. Kuparihiukkaset päällystettiin lisäksi hiilellä ja hiilinanoputkimaisilla rakenteilla lisäämällä eteeniä ja vettä reaktoriin. Kun eteenipitoisuus kasvaa nollasta 9,2 mooliprosenttiin kobolttihiukkasten LKH pienenee 84 nanometristä 17 nanometriin. Hiukkasten massakonsentraatio oli 10 g/m3 tai suurempi. Kun hiukkasen LKH oli 84 nm, oli keskihajonta 17 nm. Kun LKH oli 17 nm, oli hajonta puolestaan 7 nm. Kuparin kohdalla LKH pieneni 121 nanometristä ilman eteeniä 20 nanometriin, kun eteenipitoisuus nousi 9,2 mooliprosenttiin. Kaikissa tapauksissa hiukkaset olivat kiteisiä ja kiderakenne oli FCC. Hiukkasten muodostumisprosessia mallinnettiin yksinkertaisella laskennalla. Vaikuttaa siltä, että pintareaktiolla on tärkeä osa hiukkasten kasvussa. Ensin muodostuvat hiukkasten ytimet kaasufaasireaktiolla ja nukleaatiolla. Sitten hiukkaset kasvavat kondensaatiolla ja pintareaktiolla. Kaasufaasissa tapahtuu myös jonkin verran käänteisreaktiota metallista metallikloridiin. Sekä kobolttihiukkasten että hiilipäällystettyjen kobolttihiukkasten saturaatiomagnetisaatio vaihteli välillä 141–147 emu/g. Koboltin ominaissaturaatiomagnetisaatio on 159 emu/g. Mitatuilla hiukkasilla ei havaittu hystereesiä. Sekä hiilipäällystettyjä että päällystämättömiä kobolttihiukkasia käytettiin polymeerikomposiitin valmistuksessa. Komposiittia voidaan hyödyntää RF-antennin alustana. Komposiitin suhteellinen permeabiliteetti kasvoi arvosta 1 arvoon 3, kun hiukkasten osuus kasvoi nollasta 28 tilavuusprosenttiin. Hiilellä ja hiili-hiilinanoputkiyhdistelmällä päällystettyjä kuparihiukkasia käytettiin valmistettaessa mustetta, jolla tehtiin johtavia viivoja tulostamalla yksi kerros mustesuihkutulostuksella. Paras johtavuus oli 6,4 S/m.
ISBN, ISSN	ISBN 978-951-38-8007-1 (nid.) ISBN 978-951-38-8008-8 (URL: http://www.vtt.fi/publications/index.jsp) ISSN-L 2242-119X ISSN 2242-119X (painettu) ISSN 2242-1203 (verkkojulkaisu)
Julkaisuaika	Elokuu 2013
Kieli	Englanti, suomenkielinen tiivistelmä
Sivumäärä	62 s. + liitt. 51 s.
Avainsanat	Cobalt, copper, nickel, nanoparticles, core-shell, magnetic nanoparticles
Julkaisija	VTT PL 1000, 02044 VTT, Puh. 020 722 111

Production of Co, Ni, and Cu nanoparticles by hydrogen reduction

In this thesis, production of Co, Ni, and Cu nanoparticles by hydrogen reduction of metal chlorides in gas phase was studied. The Co and Cu particles were coated in-situ with carbon, by adding ethene to the reaction flow. Copper particles were also coated with carbon and carbon nanotube-like structures by adding ethene and water to the reaction flow. The particle growth was modelled in a simplified way.

Nanoparticles have unique properties not found in bulk or micron-scale materials. These enable new products or reduced use of raw materials. In this thesis, cobalt particles with and without carbon coating were used to fabricate polymer composites, which could be applied in RF antennae. Copper particles coated with carbon coating and CNT-like structures were used to fabricate inkjet fluid capable of producing conductive lines.

The hydrogen reduction method used in this thesis combines many favourable properties. The production rate is high and the production costs low. The primary particle size distribution can be tailored and the particle quality is high.

ISBN 978-951-38-8007-1 (Soft back ed.)
ISBN 978-951-38-8008-8 (URL: http://www.vtt.fi/publications/index.jsp)
ISSN-L 2242-119X
ISSN 2242-119X (Print)
ISSN 2242-1203 (Online)